Cartilage lacuna-biomimetic hydrogel microspheres endowed with integrated biological signal boost endogenous articular cartilage regeneration

Hao Li [a,b,c,d,1], Tianyuan Zhao [b,e,1], Zhiguo Yuan [f,1], Tianze Gao [a,b], Yongkang Yang [a,b], Runmeng Li [a,b], Qinyu Tian [b], Peifu Tang [a,c,d,**], Quanyi Guo [a,b,*], Licheng Zhang [c,d,***]

[a] School of Medicine, Nankai University, Tianjin, China
[b] Institute of Orthopedics, The First Medical Center, Chinese PLA General Hospital, Beijing Key Lab of Regenerative Medicine in Orthopedics, Key Laboratory of Musculoskeletal Trauma & War Injuries PLA, No. 28 Fuxing Road, Haidian District, Beijing, China
[c] Department of Orthopedics, The Fourth Medical Center, Chinese PLA General Hospital, Beijing, China
[d] National Clinical Research Center for Orthopedics, Sports Medicine & Rehabilitation, Beijing, China
[e] Department of Orthopaedics, Beijing Key Laboratory of Spinal Disease Research, Peking University Third Hospital, Beijing, China
[f] Department of Bone and Joint Surgery, Renji Hospital, School of Medicine, Shanghai Jiaotong University, Shanghai, China

ARTICLE INFO

ABSTRACT

Despite numerous studies on chondrogenesis, the repair of cartilage—particularly the reconstruction of cartilage lacunae through an all-in-one advanced drug delivery system remains limited. In this study, we developed a cartilage lacuna-like hydrogel microsphere system endowed with integrated biological signals, enabling sequential immunomodulation and endogenous articular cartilage regeneration. We first integrated the chondrogenic growth factor transforming growth factor-β3 (TGF-β3) into mesoporous silica nanoparticles (MSNs). Then, TGF-β3@MSNs and insulin-like growth factor 1 (IGF-1) were encapsulated within microspheres made of polydopamine (pDA). In the final step, growth factor-loaded MSN@pDA and a chitosan (CS) hydrogel containing platelet-derived growth factor-BB (PDGF-BB) were blended to produce growth factors loaded composite microspheres (GFs@μS) using microfluidic technology. The presence of pDA reduced the initial acute inflammatory response, and the early, robust release of PDGF-BB aided in attracting endogenous stem cells. Over the subsequent weeks, the continuous release of IGF-1 and TGF-β3 amplified chondrogenesis and matrix formation. μS were incorporated into an acellular cartilage extracellular matrix (ACECM) and combined with a polydopamine-modified polycaprolactone (PCL) structure to produce a tissue-engineered scaffold that mimicked the structure of the cartilage lacunae evenly distributed in the cartilage matrix, resulting in enhanced cartilage repair and patellar cartilage protection. This research provides a strategic pathway for optimizing growth factor delivery and ensuring prolonged microenvironmental remodeling, leading to efficient articular cartilage regeneration.

1. Introduction

Articular cartilage (AC) is a specialized connective tissue that enables smooth joint movement by distributing motion-related loads and minimizing friction between adjoining bones [1,2]. However, the repair of injured or degenerating articular cartilage remains a significant clinical challenge. This challenge is attributed to the avascular and aneural properties of cartilage, which restrict its innate healing abilities [3,4]. Notably, severe joint degeneration can occur in minor cartilage defects, potentially leading to osteoarthritis [5]. While advancements in treatment options have been documented, current therapeutic methods, such as autologous chondrocyte transplantation, microfracture, and

mosaicplasty, often fall short. They do not fully replicate the structure and function of healthy articular cartilage and are hampered by issues such as tissue scarcity, donor site complications, mechanical shortcomings, and host immune responses [6,7]. The establishment of a standardized treatment for cartilage injuries and the development of new solutions are complicated by the intricate nature of cartilage biology and its repair mechanisms. These mechanisms function within a constantly changing system filled with numerous interdependent factors. Hence, a universal solution for cartilage repair may not ensure clinical efficacy, suggesting that a multifaceted therapeutic strategy might be more effective.

Cartilage lacunae are spaces distributed within the cartilage matrix that partition chondrocytes into clusters [8]. The lacunae provide a mechanical microenvironment and shape chondrocytes through biomechanical signals. Restoring the lacunar structure of cartilage may aid chondrocytes in maintaining long-term biological activity [9]. Additionally, accumulating evidence suggests that the sequential introduction of activating molecules that are aligned to coordinate the tissue repair cascade can enhance repair effectiveness [10–13]. Thus, multidrug strategies that mimic natural pathological processes through sequential release are essential. Designing an integrated system equipped with multiple therapeutic functions tailored to the natural repair sequence after cartilage damage is a promising avenue. The optimal endogenous cartilage healing process encompasses hemostasis, inflammation, and remodeling (which includes the recruitment of endogenous (mesenchymal stem cells) MSCs from nearby niches, proliferation, chondrogenesis, matrix deposition, and maturation) [14].

Traditional approaches often involve loading distinct biomolecules into various biomaterials. However, these systems frequently necessitate intricate fabrication methods and the use of potentially harmful chemical agents. Such processes can diminish the bioactivity of the biomolecule, hindering its ability to authentically replicate natural cartilage. As new materials and technologies emerge, notable progress has been achieved in sequential delivery strategies addressing multiple pathological processes in cartilage repair [15–18]. For instance, in our earlier published work [19], we highlighted the capabilities of CS/MSN micro/nanospheres created via microfluidic techniques, which offer adjustable drug loading and release properties. Crucially, the entire fabrication process was conducted under straightforward and benign conditions, suggesting the potential of microfluidic methods to be further refined for the sequential delivery of biomolecules by integrating various drugs. Nevertheless, our prior research did not delve deeply into the capacity of composite microsphere-based delivery systems for the successive release of multiple agents nor did we explore how such systems might amplify the in vivo regenerative processes for chondral defects. Crafting a regenerative scaffold that boasts stable mechanical attributes alongside suitable macro/microstructures is paramount for effective cartilage defect treatment. In the absence of a well-defined macro/microporous framework, processes such as the guided homing and infiltration of endogenous MSCs, cell adhesion, proliferation, and chondrogenesis can easily become dysregulated, leading to regeneration failure [20]. As such, 3D-printed synthetic scaffolds bolstered with proregenerative biodegradable hydrogels to maintain mechanical stability at the injury site have become indispensable.

Inspired by nature, our study presents an innovative therapeutic strategy that emulates the structure of cartilage lacunae. Capitalizing on breakthroughs in hydrogel technology and insights into the pivotal roles of growth factors (GFs) in cartilage regeneration, we developed GFs loaded composite microspheres (GFs@μS). This intricate, multicomponent system creates specialized cavity spaces in the cartilage matrix, induces cellular ingrowth and enables the controlled release of GFs, directing endogenous stem cells, preventing inflammation, and promoting chondrogenesis. Our methodology involved infusing a chondrogenic growth factor, specifically transforming growth factor-β3 (TGF-β3), into mesoporous silica nanoparticles (MSNs). These nanoparticles were then enveloped in microspheres composed of polydopamine (pDA). Afterward, insulin-like growth factor 1 (IGF-1) was introduced into the pDA microspheres. Our final product merged these GF-laden MSN@pDA with a chitosan (CS) hydrogel encapsulating platelet-derived growth factor-BB (PDGF-BB), which were all assembled using microfluidic technology. We embedded our μS into an acellular cartilage extracellular matrix (ACECM) to mimic the structure of the cartilage lacunae distributed in the cartilage matrix. This material was further incorporated into a polydopamine-enhanced polycaprolactone (PCL) framework, culminating in a tissue-engineered scaffold. This work sets the stage for advanced articular cartilage repair by ensuring robust GF delivery and persistent microenvironmental adaptation (Scheme 1). The resulting strategy holds significant promise for cartilage restoration. Furthermore, our findings lay the groundwork for the development of more refined and potent cartilage repair therapies in the near future.

2. Results

2.1. Preparation and characterization of μS

Fig. 1A and B shows the morphology of the MSNs observed using SEM, revealing them as nanoscale particles. The elemental composition of the MSNs was assessed via EDS, as depicted in Fig. 1B. These findings confirmed that the MSNs were monodisperse and exhibited a highly porous structure optimal for biomolecule adsorption. The particle size distribution is shown in Fig. 1E, revealing a primary size of approximately 76 nm, largely ranging from 66 to 86 nm. Fig. 1C shows the spheroid structure of MSN@pDA, which had an average diameter of 282.37 ± 85.58 nm, as shown in Fig. 1E. TEM was employed to obtain additional insights, and Fig. 1D displays the uniform distribution of MSNs within the pDA microspheres, exhibiting a well-ordered spheroid structure. The modified structure after pDA introduction, as evident from the absence of a channel structure and the presence of a polymer shell, was also distinctly observed. FTIR spectroscopy images (Fig. 1F) revealed new absorption peaks in the spectrum of MSN@pDA, specifically between 1400 and 1500 cm^{-1}, attributed to benzene ring vibrations. The loading efficiencies of TGF-β3, IGF-1, and PDGF-BB were 75.04 ± 0.70 %, 64.17 ± 0.19 %, and 92.28 ± 0.09 %, respectively (Table S1).

The CS/MSN and CS/MSN@pDA μS were characterized via SEM and TEM (Fig. 1H). SEM images show the surface and cross-sectional morphologies of the μS. Both types of μS structures were notably similar, as shown in Fig. 1G, which shows their average diameter distributions. TEM images of their internal structures are provided in Fig. 1H. As evident from TEM images, MSNs were interspersed throughout the CS/MSN μS. CS/MSN@pDA μS exhibited clear MSN@pDA aggregation, confirming the successful creation of cartilage lacuna-biomimetic hydrogel microspheres. The FTIR spectra (Fig. 1I) of these μS showed characteristic peaks associated with CS components. The reduced intensity of the characteristic absorption peak of the MSNs in the CS/MSN μS suggested that the MSNs were uniformly dispersed within the CS microspheres.

Upon immersion in deionized water, the lyophilized porous CS/MSN and CS/MSN@pDA μS exhibited significant swelling, reaching a plateau after 9 h (Fig. 1J). The high swelling capacity of these materials enhanced their drug-loading potential, particularly for PDGF-BB. The critical degradation of these porous hydrogel microspheres plays a vital role in GF release. As depicted in Fig. 1K, the CS/MSN residual weight generally decreased over time, from 25.9 ± 1.6 % (week 4) to 3.62 ± 0.4 % (week 8) (Fig. 1K), while the mass of CS/MSN@pDA decreased from 42.2 ± 5.7 % (week 4) to 4.95 ± 0.9 % (week 8). However, CS/MSN@pDA μS showed a more gradual degradation rate, potentially due to the integrated structure of pDA and CS. We proposed a multilayer package assembly strategy to enable the loading of multiple GFs onto the μS. After gradient slow release, the GFs further facilitate endogenous MSCs migration, proliferation, and chondrogenesis. The release profile of GF-loaded μS was investigated to verify our hypothesis. In the release
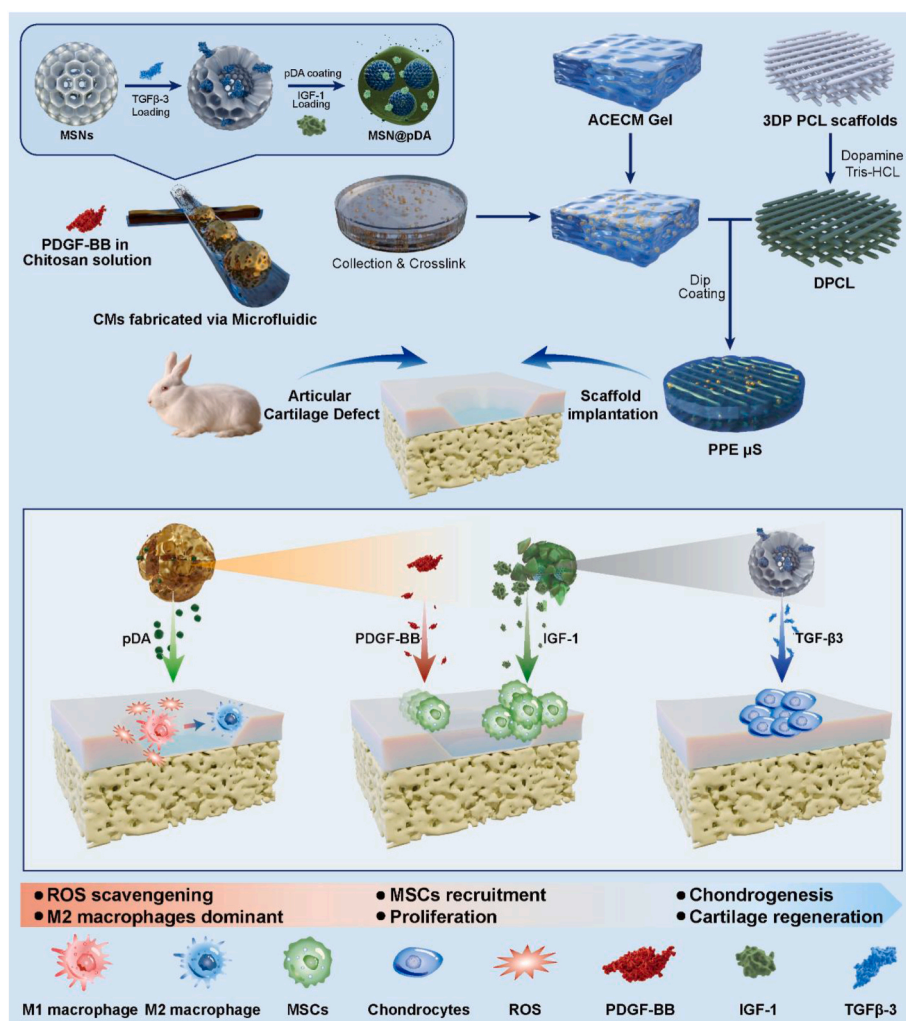
Scheme 1. Schematic illustrations of the cartilage lacuna-biomimetic hydrogel microspheres-containing scaffold and its application as a multifunctional therapeutic for cartilage regeneration. The TGFβ3-loaded MSN@pDA microspheres incorporated with IGF-1 via the self-polymerization process of pDA, and combined with PDGF-BB to fabricate µS by using microfluidic technology. The functional PPE µS scaffold was further developed through incubation with GFs@µS and implanted into articular cartilage defects. The PPE µS scaffold programmed reprogramming macrophage activities, scavenging ROS, recruiting MSCs and promoting MSCs proliferation, and enhancing chondrogenesis and AC regeneration.

profile, a burst release occurred in the first week, with a total amount of 64.0 ± 3.4 % for PDGF-BB, 50.9 ± 1.9 % for IGF-1, and 35.5 ± 0.7 % for TGF-β3. By the end of week 4, the cumulative release of PDGF-BB was 88.1 ± 3.6 %, that of IGF-1 was 81.4 ± 1.5 %, and that of TGF-β3 was 63.3 ± 1.4 % (Fig. 1L). These findings suggest that our multilayer packaging approach can effectively orchestrate the release of GFs with multiple functions, potentially enhancing reparative activity by facilitating endogenous MSCs recruitment, proliferation, and chondrogenesis.

2.2. Characterization of the PPE µS scaffold

Macro- and microstructure images are shown in Fig. 2A and B. Following surface modification with pDA, the appearance of the scaffold transitioned to a black hue. The post-modification PCL framework displayed an N signal in the EDS map (Fig. S1). Structural geometry analysis, performed through stereomicroscopy and SEM, revealed a heterogeneous distribution of macro- and micropores. EDS mapping validated the integration of µS into the PPE scaffold (Fig. S2). The micropores of the PPE and PPE µS scaffolds primarily ranged between 77-129 µm and 83–141 µm (Fig. 2E), respectively, fostering cell adhesion, retention, and differentiation. The scaffold porosity was 69.43 ± 4.77 %

for the PPE scaffold and 61.48 ± 1.88 % for the PPE µS scaffold (Fig. 2F). µS exhibited a scattered arrangement on the scaffold, and Fig. 2B illustrates the microstructures of both µS and the scaffold. Surface modification of the PCL scaffold through the oxidation self-polymerization of PDA in an alkaline solution enhanced its hydrophilicity to promote cell attachment [21]. The contact angle of the PPE scaffold was 45.63 ± 2.72°, while that of the PPE µS scaffold was 29.07 ± 4.71°, signifying a notable improvement in hydrophilicity conducive to enhanced cell attachment (Fig. 2C and D).

In the realm of tissue-engineered cartilage scaffolds, inadequate mechanical attributes frequently culminate in suboptimal repair outcomes. Consequently, we probed the biomimetic mechanical properties of the scaffolds under compression. The compressive moduli were computed from the slope of the linear region of the stress–strain curve (Fig. 2G and H). Both the PPE and PPE µS scaffolds exhibited compressive moduli of 7.098 ± 1.3837 and 7.489 ± 1.1995 MPa, respectively, indicating favorable mechanical performance compared to native articular cartilage (compressive modulus: ~6 MPa) [22]. No significant differences emerged between these scaffolds (Fig. 2I). Biocompatibility assessments were conducted through live/dead cell staining and DAPI/F-actin staining. Confocal microscopy revealed an abundance of live cells (green) with few dead cells (red) across all
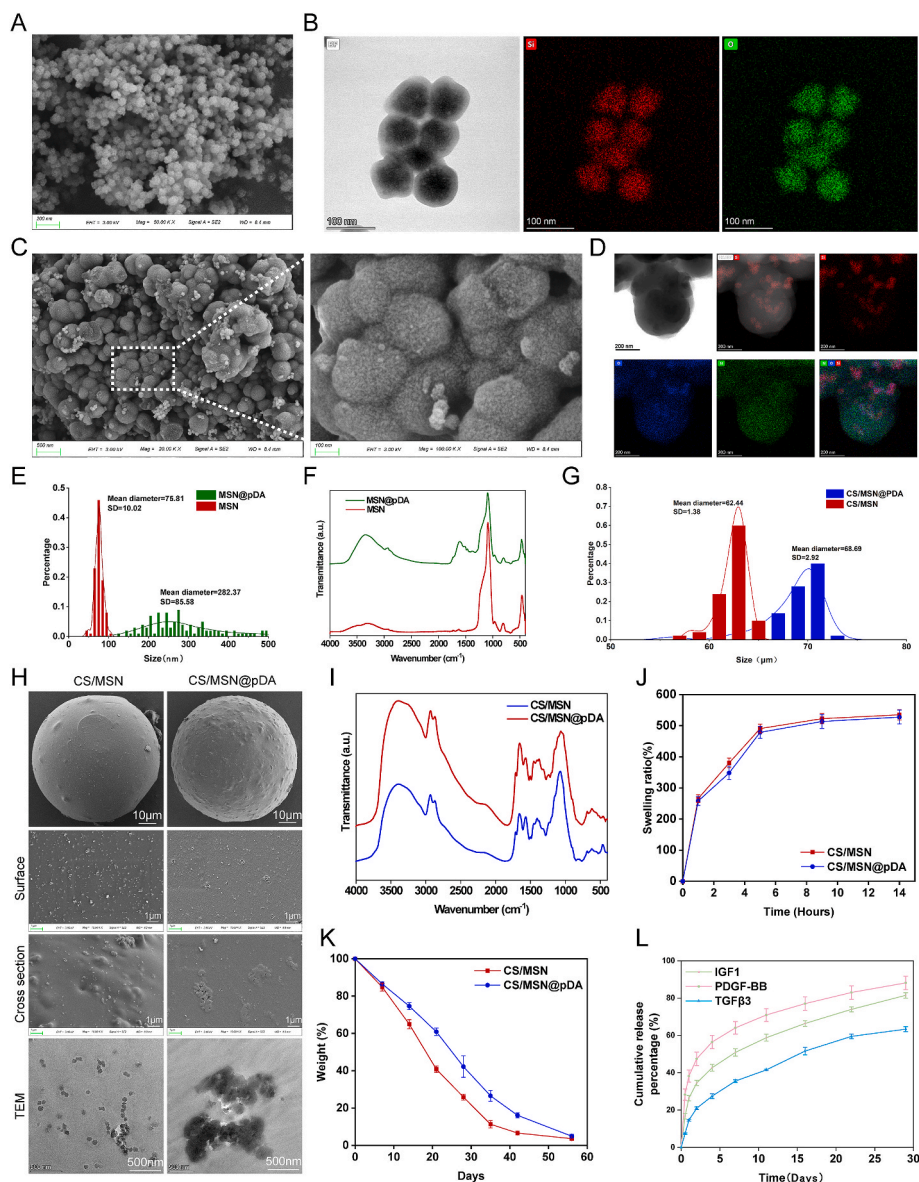
Fig. 1. Characterization of μS. A) SEM image of MSNs. B) TEM images and elemental mapping images of MSNs. (Silicon (Si) map; oxygen (O) map). C) SEM images of pDA microspheres. D) TEM images of pDA microspheres and elemental mapping images of pDA microspheres. (silicon (Si) map; oxygen (O) map; nitrogen (N) map). E) Distribution of the diameters of MSNs and pDA microspheres. F) FTIR spectra of MSNs and MSN@pDA. G) Distribution of the diameters CS/MSN and CS/MSN@pDA. H) SEM images of μS, surface cross section, and TEM image of the cross section. I) FTIR spectra of different microspheres. J) Swelling ratio profiles of different microspheres. K) The degradation curve of μS over time. L) In vitro profiles of TGF-β3, IGF-1 and PDGF-BB released from GFs@μS.

scaffolds, indicating conducive microenvironments for cell growth (Fig. 2J). No notable difference in live cell counts was observed between the two scaffold types (Fig. S3). Furthermore, DAPI/F-actin staining revealed diverse cell stretching characteristics within each group (Fig. 2K). SEM images also showed favorable cell adhesion on both scaffold types (Fig. S4). These combined results underscored the commendable biocompatibility of the PPE and PPE μS scaffolds and their capacities to provide an optimal platform for cell adhesion, proliferation, and spreading following migration.

### 2.3. Anti-inflammatory and immunomodulatory effects of μS

Within the intra-articular environment, macrophages undergo differentiation into proinflammatory (M1) and anti-inflammatory (M2) phenotypes. While M1 macrophages steer the inflammatory response during the inflammatory phase of cartilage repair, M2 macrophages play pivotal roles in immune regulation and tissue remodeling [23].

Facilitating the transition from the M1 to M2 phase in macrophages can effectively curb persistent inflammation and promote the intrinsic healing of cartilage. We evaluated macrophage polarization using immunofluorescence staining, flow cytometry, and RT−qPCR analysis to confirm the immunomodulatory effects of μS in vitro (Fig. 3A–C). Immunofluorescence staining (Fig. 3A) revealed that CD86 expression increased significantly upon LPS induction, and the expression of the M1-related marker CD86 in the CS/MSN@pDA-3 treatment group was lower than that in the other three groups, while the expression of the M2-related marker CD206 was higher. The RT−qPCR analysis revealed a decrease in the expression of the M1-related genes inducible nitric oxide synthase (iNOS) and CD86 with increasing CM concentrations, while the expression of the M2-related genes Arg-1 and CD206 increased (Fig. 3B). Flow cytometry analysis of macrophage phenotypes (Fig. 3C) indicated that the percentage of CD163$^+$ macrophages increased from 14.0 % to 26.5 % after treatment with CS/MSN@pDA-3 μS. Notably, the CS/MSN@pDA-3 group displayed the highest M2/M1 ratio, indicating
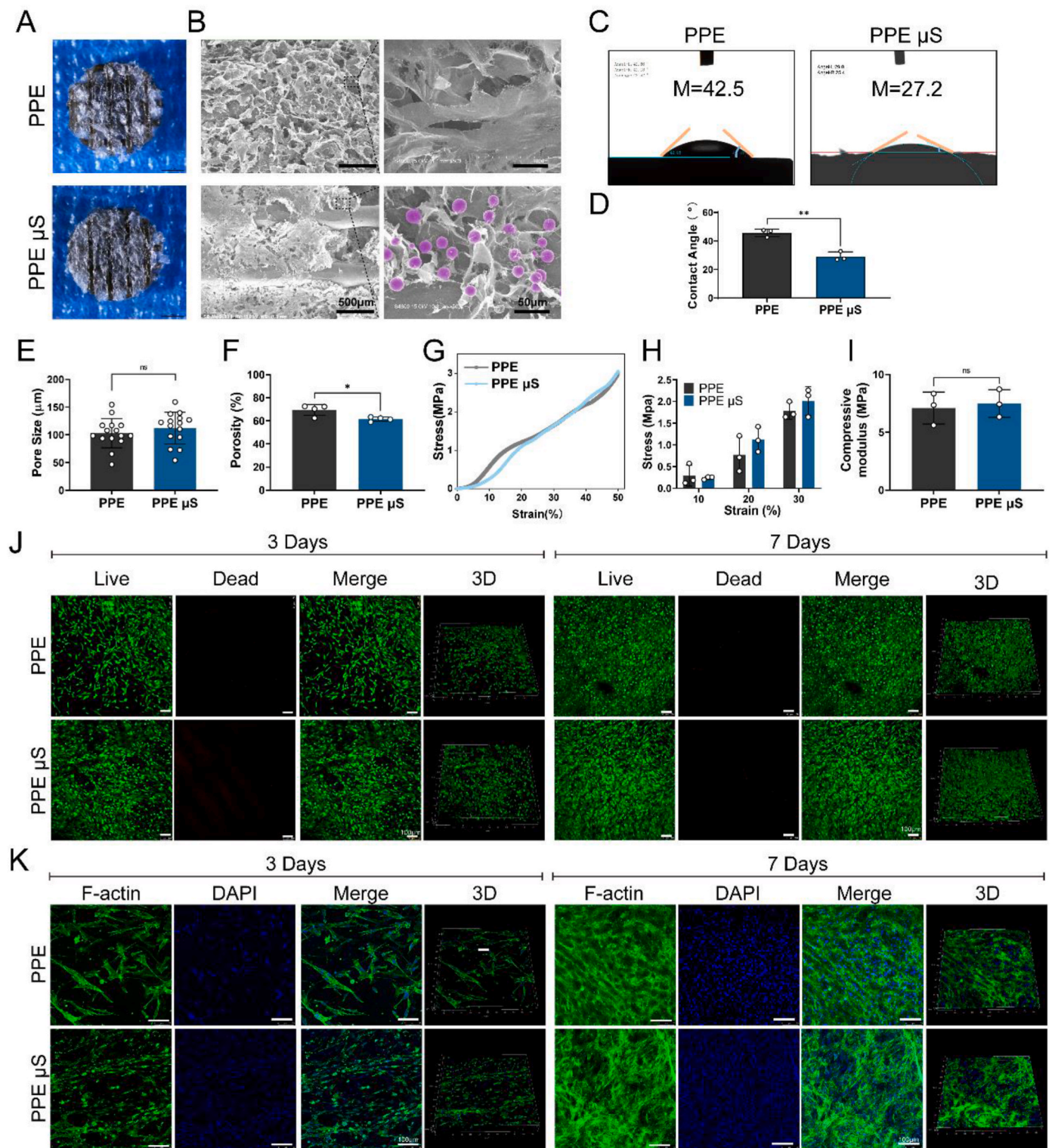
Fig. 2. Characterization of the composite scaffolds. A) Macroscopic photographs of the PPE and PPE μS scaffolds. B) SEM image of μS in the scaffold. This image was further reproduced, and the μS were marked by pseudocoloring for better visualization (purple: μS). C) Water contact angle observations for the PPE and PPE μS scaffolds. D) Water contact angles of different scaffolds (n = 3 per group). E) Average pore sizes of the different scaffolds. F) Porosity of different scaffolds. G) Stress−strain curves and H) instantaneous compressive stress and I) modulus of the PPE and PPE μS scaffolds. J) Live/dead staining and three-dimensional fluorescence images of SMSCs on the scaffolds after 3 days and 7 days of culture. K) Cell adhesion on the PPE and PPE μS scaffolds. The data are shown as the means ± SDs; *p < 0.05 and **p < 0.01.
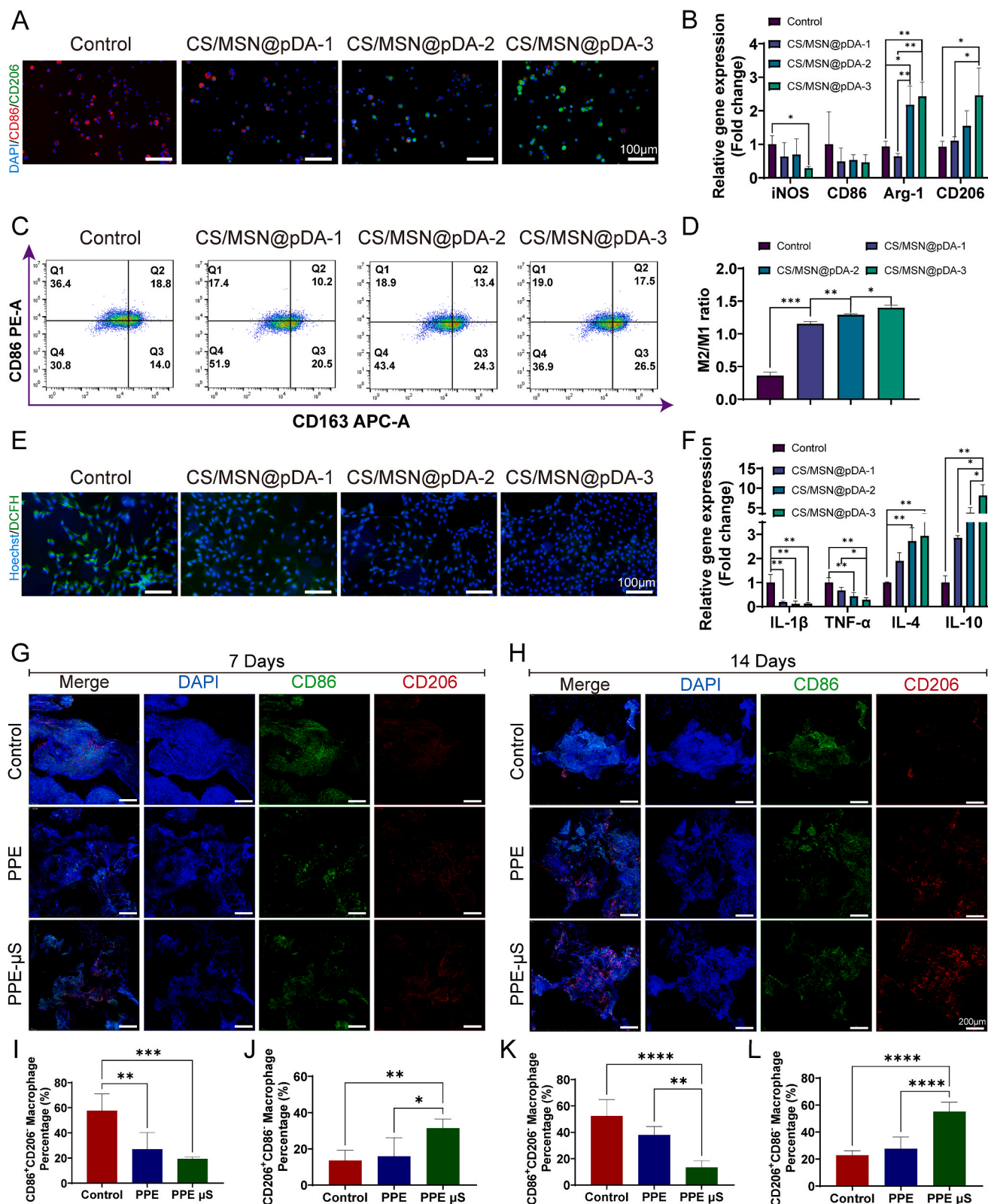
Fig. 3. Dose-dependent and immunomodulatory effects of μS and scaffolds in vitro and in vivo. A) Intensity of CD86/CD206 immunofluorescence staining. B) qPCR-determined levels of the iNOS, CD86, Arg-1, and CD206 genes expression. C) Representative flow cytometry results showing the percentages of CD86⁻ and CD163-positive cells, representing M1 and M2 macrophages, respectively. D) Statistical analysis of the results of flow analysis. E) Intracellular ROS detection with the DCFH-DA probe. F) RT−qPCR was used to determine the gene expression levels of IL-1β, TNF-α, IL-4, and IL-10. G-H) Intensity of dual CD86/CD206 immunofluorescence staining at 7 days and 14 days post-implantation. I-L) Statistical analysis of the percentages of M1 (I, K) and M2 (J, L) macrophages. The data are shown as the means $\pm$ SDs; *$p < 0.05$, **$p < 0.01$, ***$p < 0.005$, and ****$p < 0.001$.

that this group is capable for modulate macrophages phenotypes and promising for cartilage regeneration (Fig. 3D).

DCFH-DA staining and RT−qPCR analysis were used to assess chondroprotective effects on chondrocytes (Fig. 3E and F). The ability of μS to scavenge intracellular ROS was gauged using DCFH-DA probes to label ROS within chondrocytes subjected to different μS scaffolds (Fig. 3E). Enhanced fluorescence quenching, proportional to the CM mass, was observed compared to that in the positive control group, with CS/MSN@pDA-3 exhibiting the most substantial decrease in fluorescence intensity. The expression of the IL-1 and TNF-α genes decreased significantly in the CS/MSN@pDA-3 group compared with the other groups (Fig. 3F). Remarkably, the CS/MSN@pDA-3 treatment group exhibited a discernible anti-inflammatory effect compared to that of the non-μS treatment group. Nonetheless, the anti-inflammatory effects of the CS/MSN@pDA-1 and the non-μS treatments were not substantially different. The expression patterns of the IL-4 and IL-10 genes displayed opposite patterns to those of IL-1 and TNF-α. The cumulative findings confirmed that the anti-inflammatory effects on chondrocytes and macrophage polarization responses were reliant on μS concentrations within a specific range. Consequently, CS/MSN@pDA-3 was selected as the appropriate μS loading dose for subsequent integration into the PPE scaffold.

The immunomodulatory efficacy of the PPE μS scaffold was further confirmed in vivo (Fig. 3G-L). Compared with those in the control group, the M1 and M2 macrophage populations were notably augmented on days 7 and 14 after the cartilage defect (Fig. 3G-L). Initially, a more substantial M1 macrophage population (green, CD86-positive) was identified in the control group (57.7 %) after 7 days, signifying a proinflammatory response following PPE scaffold implantation. In contrast, the percentage of M1 macrophages in repaired tissue treated with PPE μS scaffolds (19.4 %) was significantly lower than that in the PPE and control (27.1 %) groups (Fig. 3G). Furthermore, the percentage of M2 macrophages (red, CD206-positive) (31.4 %) in repaired tissue treated with the PPE μS scaffold was greater than that in the PPE (15.9 %) and control (13.5 %) groups (Fig. 3I and J). Similar trends were detected using immunostaining for CD86 and CD206 after 14 days (Fig. 3K-L). Notably fewer M1 macrophages were observed in regenerated tissue treated with PPE μS scaffolds (13.4 %) and PPE scaffolds (37.9 %) than in control tissue (52.4 %). Additionally, the proportion of M2 macrophages in regenerated tissue treated with PPE μS scaffolds (55.0 %) surpassed that in regenerated tissue treated with PPE scaffolds (27.6 %) and control tissues (22.8 %) (Fig. 3L). In essence, scaffolds enriched with the ECM biomimetic and immunomodulatory μS, which have high macrophage affinity, led to amplified macrophage phenotypic shifts, primarily toward the M2 type. These findings underscore the robust macrophage polarization potential of PPE μS scaffolds.
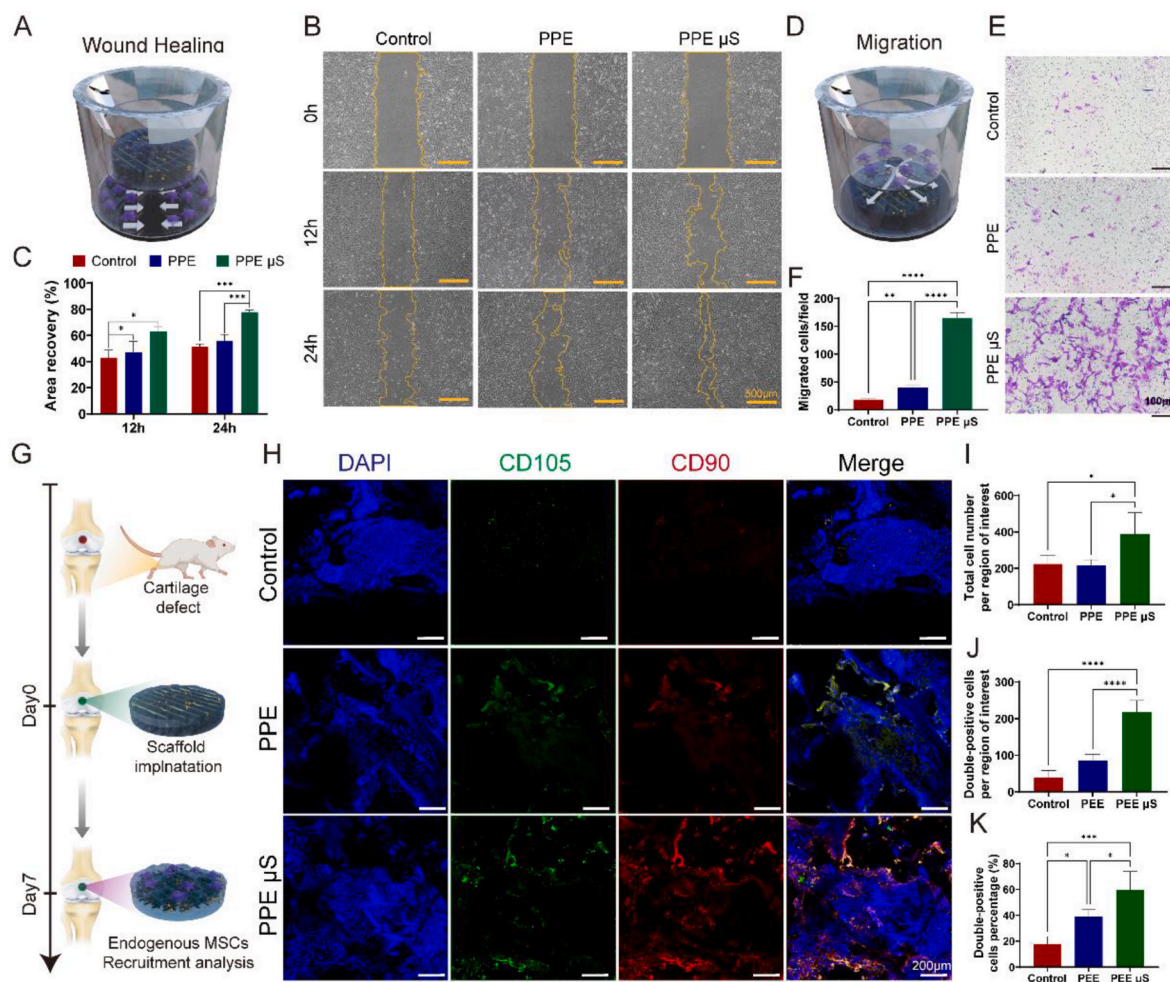
Fig. 4. Scaffolds loaded with GFs@μS promoted cell migration both in vitro and in vivo. A) Schematic diagrams of the wound healing assay. B) Microscopy images of the scratch wounds in different groups at 0, 12, and 24 h. C) Statistical analysis of the recovery area in the wound healing assay. D) Schematic diagrams of the Transwell cell migration assay. E) Transwell assay of SMSCs migration in vitro. F) Quantitative analysis of cell counts in the Transwell assay. G) Schematic diagrams of the in vivo endogenous MSCs recruitment assay. H) Confocal images of MSCs recruitment to different scaffolds in vivo. I) The total number of cells that migrated to the defect. J) The number of CD105 and CD90 double-positive cells recruited to the defect. K) The percentage of double-positive cells among the total cells. The data are shown as the means ± SDs; n = 3. *p < 0.05, **p < 0.01, ***p < 0.005, and ****p < 0.001.

2.4. GFs@µS promoted the migration of synovium-derived MSCs (SMSCs) both in vitro and in vivo

The pivotal role of sufficient and specific endogenous MSCs in effective cartilage repair cannot be overstated, as an inadequate presence of MSCs might hinder the healing process [24,25]. In this context, we explored the impact of GF-loaded µS on the recruitment and mobilization of MSCs both in vitro and in vivo. Firstly, we conducted wound healing experiments (Fig. 4A) and Transwell assays (Fig. 4D) in vitro to investigate the effects of the PPE and PPE µS scaffolds on SMSCs migration. As illustrated in Fig. 4B, compared with control cells, cells treated with both PPE and PPE µS scaffolds exhibited more rapid coverage of the scratched area. However, the influence of the PPE µS scaffold treatment appeared more pronounced than that of the PPE treatment, highlighting the superior ability of PPE µS scaffolds to promote SMSCs migration in vitro. A statistical assessment of the scratch width further validated the accelerated healing exhibited by the PPE µS group (Fig. 4C). Transwell assays were subsequently conducted to assess SMSCs migration in vitro. After the PPE µS scaffold was placed beneath the Transwell inserts, crystal violet histological staining revealed a uniform distribution of migrated cells (Fig. 4E). After a 24-h incubation, both the PPE and PPE µS groups displayed significantly greater numbers of migrated SMSCs than did the control group (Fig. 4E and F). In summary, these findings collectively revealed the ability of the PPE µS scaffold to enhance MSCs recruitment and mobilization.

While the in vitro results established the SMSC-specific recognition and recruitment capabilities of PPE µS scaffolds, their in vivo MSCs recruitment ability remains an enigma. Hence, we evaluated migration in vivo by implanting a PPE µS scaffold within rat cartilage and harvesting the tissue at 1 week post-surgery (Fig. 4G). Confocal imaging unequivocally revealed that the total cell numbers in the meniscal defects of both scaffold groups surpassed those in the control group (Fig. 4H–K). Furthermore, the total cell numbers in the PPE µS group were greater than those in the PPE group, although no substantial difference was noted compared to the PPE group or control group. This observation underscored the role of GFs released from the µS, rather than the scaffold itself, in fostering cell migration (Fig. 4I). Importantly, CD90 and CD105 were selected as dual MSC-specific markers to discern endogenous stem cells migrating to the defects. The results showed that the number of CD90/CD105 double-positive cells in the PPE µS group significantly exceeded that in the control and PPE groups (Fig. 4J and K). Thus, these in vivo outcomes indicated the ability of PPE µS scaffolds to accurately capture endogenous MSCs and facilitate their targeted migration toward cartilage defect sites during regeneration.

2.5. Effect of GFs@µS on the proliferation and chondrogenic differentiation of SMSCs

We conducted two assays to elucidate the impact of PPE µS scaffolds on SMSCs proliferation. First, we employed CCK-8 assays to explore the effects of the scaffolds on cell proliferation. The assay revealed a progressive increase in the number of SMSCs cultured on the scaffold from day 1 to day 7. Notably, the PPE scaffold group exhibited a higher cell proliferation rate than the control group. The PPE µS group exhibited the most robust growth rate among the four groups (Fig. 5A and B). Second, we used EdU staining to verify the influence of the PPE µS scaffolds on SMSCs proliferation. The results of the EdU analysis (Fig. 5C–E) further confirmed that the number of EdU-positive SMSCs observed following treatment with PPE µS scaffolds exceeded that in the PPE and control groups. In summary, these findings demonstrated the capacity of PPE µS scaffolds to effectively promote SMSCs proliferation.

Our investigation of SMSCs chondrogenic differentiation was performed utilizing a pellet culture system, a method aligned with established research practices [19]. Specifically, we evaluated the potential of both PPE and PPE µS scaffolds to induce chondrogenic differentiation in SMSCs pellet cultures employing the Transwell system (Fig. 5F). The

pellet morphology exhibited remarkable similarity (Fig. 5G). Histological examinations through H&E staining revealed that the PPE µS scaffold-treated pellets exhibited a profusion of chondrocyte-like cells and well-defined cartilage lacunae. In contrast, PPE-treated pellets exhibited a predominance of spindle-shaped cells and a less organized structure. Higher intensity Alcian blue (AB) and Safranin O/Fast Green (SO/FG) staining was observed in pellets treated with PPE µS scaffolds than in those treated with PPE scaffolds (Fig. 5H). We performed a quantitative analysis of key chondrogenic-related differentiation markers, including collagen type II (COL2), (SRY-box transcription factor 9) SOX9, and aggrecan (ACAN), at the gene level to further clarify the role of PPE µS scaffolds in promoting chondrogenic differentiation in SMSCs. Using RT-qPCR, we determined the expression levels of these markers in SMSCs treated with PPE µS scaffolds for 7 and 14 days. Impressively, the PPE µS scaffold significantly upregulated the expression of chondrogenesis-specific genes (Fig. 5I). Moreover, we assessed the expression of the COL1 gene and noted no substantial difference between the two scaffold groups after 7 days of differentiation. However, at the 14-day time point, the PPE µS scaffolds significantly decreased COL1 expression (Fig. 5I). In summary, these compelling outcomes collectively underscore the potent role of PPE µS scaffolds in fostering the chondrogenic differentiation of SMSCs.

Modulation of the macrophage phenotype can exert chondroprotective effects and potentially accelerate cartilage repair [26]. Therefore, we examined the protective effects of condition medium (CM) from macrophages exposed to different scaffolds on chondrocytes. The results of chondroprotective immunofluorescence staining, as depicted in Fig. 5J and K, highlight the alterations in IL-1β and MMP-13 levels in cells from different groups following pretreatment with IL-1β. IL-1β, a proinflammatory factor, induces MMP-13 expression, leading to cartilage matrix degradation, chondrocyte injury, and potential apoptosis. Over a 3-day culture period, the fluorescence intensity of IL-1β and MMP-13 exhibited a progressive decline in the control, PPE-CM, and PPE µS-CM groups. Remarkably, the PPE µS-CM group displayed minimal fluorescence signals, indicating the potent inhibitory effect of the GFs@µS-loaded scaffold on the inflammatory microenvironment, thereby protect chondrocytes.

2.6. GFs@µS regulate the fate of SMSCs in vitro

An illuminating exploration of the mechanisms that steer MSCs fate was undertaken through an mRNA-seq analysis of the cell–PPE µS composite. Specifically, SMSCs cultivated within PPE and PPE µS scaffolds were compared after 21 days of chondrogenic induction (Fig. 6A). Principal component analysis (PCA) showed a clear demarcation between all genes within the PPE µS group and those within the control PPE group, underscoring their distinct transcriptional profiles (Fig. 6B). An impressive total of 4029 differentially expressed genes (DEGs), encompassing 1615 downregulated and 2414 upregulated genes, were identified (Fig. 6B–D). A thorough examination of the DEGs revealed significant enrichment across various biological processes, including the orchestration of cell migration and proliferation and cellular components such as lysine and purine. Moreover, the analysis of DEGs revealed pivotal signaling pathways, including the TGF beta, PI3K-Akt, MAPK, JAK-STAT, NOD-like, NF-kappa B, and ferroptosis pathways (Fig. S5). Notably, the candidates included genes associated with cell adhesion (Nuak1 and Has1), cell migration (Nedd9), and negative regulation of cell death (Ier3, Phlda1, and Gclm) (Fig. S5B). The scope of GO functions inherent to DEGs in the context of cartilage regeneration was further dissected into categories such as extracellular matrix modulation and immune regulation. In this context, the GO term "extracellular matrix modulation" was significantly upregulated, whereas immune response-linked terms such as response to chemokines, lipid biosynthetic process, regulation of the inflammatory response, and neutrophil chemotaxis were downregulated (Fig. S6).

Subsequently, a bubble chart was generated for the KEGG analysis to
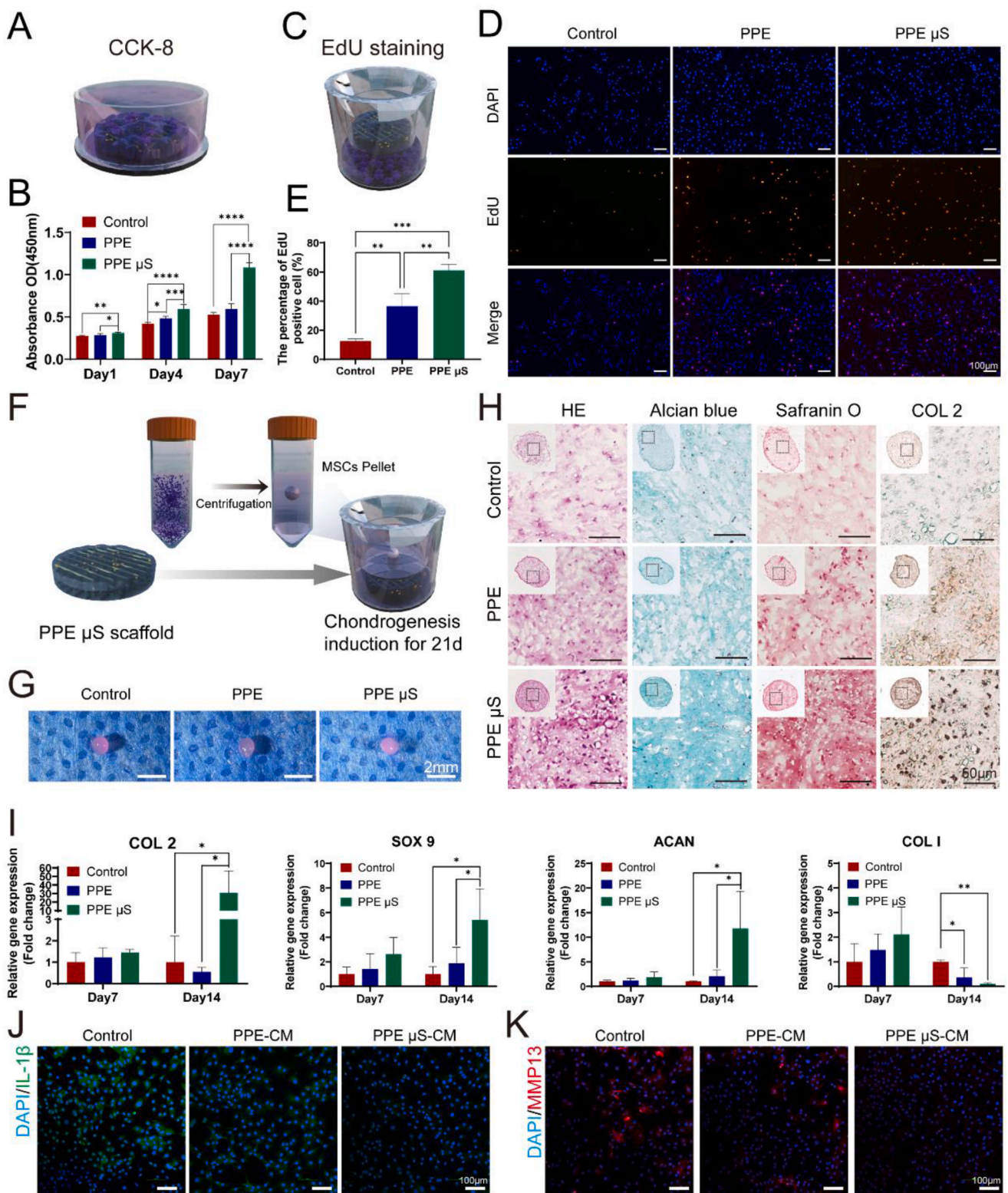
Fig. 5. Enhanced cell proliferation and chondrogenesis in vitro. A) Schematic diagrams showing SMSCs seeded on scaffolds for the CCK-8 assay. B) Statistical analysis of CCK-8 assays of SMSCs proliferation. C) Schematic diagrams showing SMSCs cocultured with the scaffold for EdU staining. D) Immunofluorescence micrographs of EdU staining (EdU: orange, nuclei: blue). E) Semiquantitative analysis of the EdU-positive cell ratio based on the images. F) The Transwell system was used to evaluate the chondrogenic differentiation effect of the PPE μS scaffolds. G) Gross observation of the pellets treated with different scaffolds. H) H&E, Alcian blue, and safranin O staining and immunohistochemical staining for COL 2 in SMSC pellets that were cocultured with different scaffolds. I) Expression of the COL 2, SOX9, ACAN, and COL 1 mRNAs in SMSCs pellets at 7 and 14 days. J) Immunofluorescence staining images of IL-1β in chondrocytes treated with different conditioned mediums. K) Immunofluorescence staining images of MMP13 chondrocytes treated with different conditioned mediums. The data are shown as the means ± SDs; *p < ,0.05 and **p < 0.01.
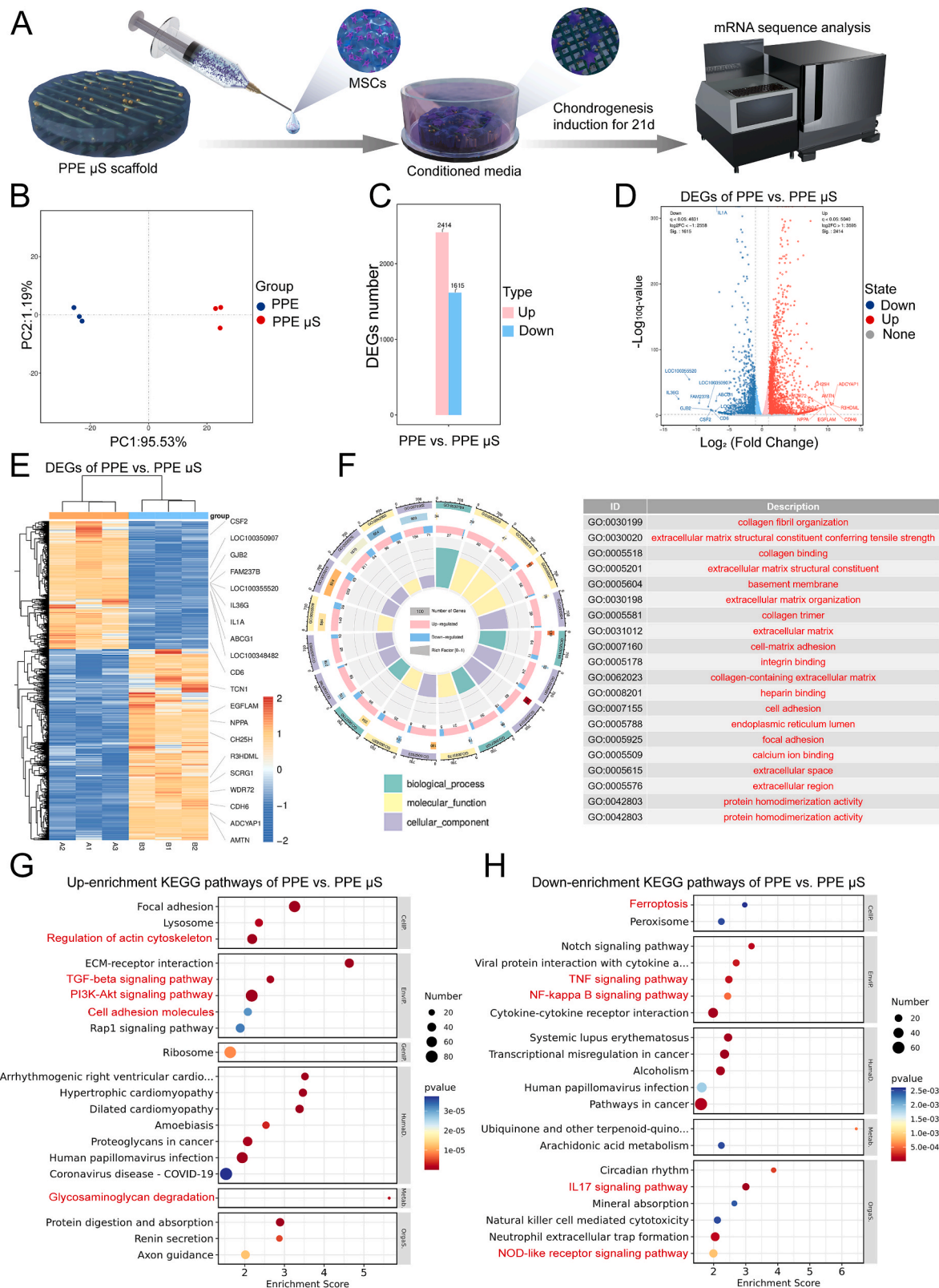
Fig. 6. Analyses of mRNA-seq data and DEGs in SMSCs cultured on different scaffolds for 21 days. A) Schematic of chondrogenic induction before mRNA-seq analysis. B) PCA of DEGs in the two groups (n = 3). C) Numbers of DEGs in the two groups. Volcano plot D) and heatmap E) of DEGs in the two groups. F) The significantly enriched GO terms for the DEGs indicated that the effects of the PPE μS scaffolds on the SMSCs were associated with cell–matrix adhesion and the extracellular matrix. G) Enriched and down-regulated H) KEGG pathways.

discern the enriched gene pathways intricately linked with cartilage growth, microenvironment modulation, and matrix metabolism. The degree of KEGG pathway enrichment was gauged based on the gene count, p value, and enrichment score. As depicted in Fig. 6G–H, a cluster of upregulated pathways, including the regulation of the actin cytoskeleton, TGF beta, PI3K-Akt, cell adhesion, and glycosaminoglycan degradation signaling pathways (Fig. 6G), were identified. Furthermore, 5 pathways related to immune regulation, including the ferroptosis, TNF, NF-kappa B, IL17, and NOD-like signaling pathways, were distinctly downregulated (Fig. 6H). GSEA was performed for TGFβ- and glycosaminoglycan degradation-related KEGG terms to explore this phenomenon in depth, and notably, these terms were substantially enriched in the PPE μS group, indicating that they are involved in cartilage repair (Figs. S7A–B). Concurrently, GSEA revealed the suppression of immune modulation- and cell apoptosis-associated pathways, such as the NF-κB and IL17 signaling pathways, thus mitigating inflammation and unexpected cell death (Figs. S7C–D). In summary, the data suggest that the PPE μS scaffold potentially advances cartilage regeneration through mechanisms involving augmented cell migration, the cessation of the immune response and cell death, and enhancement of extracellular matrix remodeling.

2.7. GFs@μS promotes the quality of repaired cartilaginous tissue

As a method to further investigate the regenerative mechanisms modulated by GFs@μS, we first applied a proteomic analysis to assess the general effect of GFs@μS on articular cartilage regeneration in vivo. In this assay, the experimental group consisted of ACECM hydrogels loaded with GFs@μS, and the control group consisted of ACECM hydrogels loaded with GFs and μS. Both types of hydrogels were implanted into the knee cartilage defects of rats, and samples were collected at 14 days post-surgery. The proteomic perspective provides us with independent information on the positive bioeffects of GFs@μS on endogenous MSCs function that transcriptomics has failed to show. PCA was performed to determine the homogeneity and heterogeneity of the different groups (Fig. 7A). A Venn diagram and volcano plot were subsequently generated, revealing that 798 proteins were upregulated and 1086 proteins were downregulated after the GFs@μS intervention compared to those in the GF group (Fig. 7B and C). Kyoto Encyclopedia of Genes and Genomes (KEGG) enrichment analysis (different) suggested that after GFs@μS treatment, the ECM-receptor interaction signaling pathway, cytokine–cytokine receptor interaction signaling pathway, and Rap1 signaling pathway were significantly different between the two groups of repaired tissues (Fig. 7D). Furthermore, the enrichment (upregulated) analysis suggested that after GFs@μS treatment, the ECM-receptor interaction signaling pathway, PPAR signaling pathway, PI3K-Akt signaling pathway, and TGF-beta signaling pathway were significantly upregulated in repaired tissue (Fig. 7E). A heatmap of the Rap1 signaling pathway-related gene cluster showed that GFs@μS upregulated the expression of the chemoattractants M-CSF1, FGF-R, and PDGF-C in repaired tissue (Fig. S8A). Clustering analysis of crucial proteins associated with the PI3K-Akt signaling pathway revealed that GFs@μS significantly upregulated the expression of the ECM-related family of genes, including COL2A1 (the main component of the cartilage ECM), fibronectin, COL6A1, LAMB2, and COMP (Fig. S8B). We further analyzed the DEPs using the STRING database to construct a protein–protein interaction (PPI) network and identified several proteins that are mainly associated with the Rap1 and PI3K–Akt pathways. Based on the correlation coefficients, we detected matrix formation proteins (such as ITGA9, COL6, THBS, FN1 and LAMB2) and matrix degeneration proteins (such as FGFR1 and IBSP) with a relatively high degree of correlation between both pathways (Fig. 7F). These results suggest that the regulation of endogenous cartilage regeneration by GFs@μS was potentially mediated by the activation of the Rap1 signaling pathway and the upregulation of the PI3K-Akt signaling pathway, reducing matrix degeneration and inflammation and thus

promoting cartilaginous matrix formation (Fig. 7G). The expression of markers such as PI3K, p-PI3K, Akt, and *p*-Akt p65 in the PI3K-Akt signaling pathway and RAP1A and RAP1-GAP in the Rap1 signaling pathway was verified via WB (Fig. 7H). We also conducted RT–qPCR analysis, as shown in Fig. 7I. The expression of the representative chondrogenesis-related mRNAs was significantly upregulated after GFs@μS treatment compared with that in the GF group, while the expression of the representative fibrous and matrix degeneration-related mRNAs was significantly downregulated by the GFs@μS intervention (Fig. 7J–K).

2.8. In vivo cartilage repair studies

An insightful in vivo study was conducted using rabbit models to assess the reparative impact of the hydrogels, leveraging their larger joints and substantial cartilage layers. The rabbits were divided into three groups—control, PPE, and PPE μS—and an experimental model of full-thickness cartilage defects was generated within the knee joint to discern the cartilage regeneration potential of the hydrogels (Fig. 8A). The reparative effects of the different scaffolds were compared at 6–12 weeks in vivo (Fig. 8B). Six weeks after scaffold implantation, macroscopic results revealed that the control group exhibited minimal new cartilage within the defects, while partial refilling was noted in the PPE and PPE μS groups. At the 12-week assessment, all groups displayed improved tissue repair and integration, albeit with distinctive interfaces against the adjacent normal cartilage. The control group exhibited uneven tissue growth with conspicuous voids. In contrast, the PPE μS group emerged as the most promising group, showing complete and smooth macroscopic outcomes and superior integration with neighboring cartilage. Employing a tailored semiquantitative scoring system for macroscopic cartilage repair further underscored the beneficial outcomes of PPE and PPE μS scaffolds for chondral defects, with the untreated group serving as the control (Fig. 8C–I). According to these scoring parameters, the PPE μS group exhibited a greater degree of cartilage repair than the PPE and control groups.

For an in-depth assessment, micro-CT was harnessed to evaluate new tissue ingrowth within the defect site, with a specific focus on new bone formation in the repair area (Fig. 8J-L). These findings revealed robust new bone generation in the PPE μS group compared to the PPE and control groups. BV/TV and BMD measurements were performed to assess subchondral bone repair after PPE and PPE μS scaffold treatment. Compared with those in the other two groups, the BV/TV in the repair zone in the PPE μS group was significantly higher (Fig. 8K). Similarly, the PPE μS group had the highest bone mineral density (BMD) (Fig. 8L), in contrast to the other groups.

Further histological and immunological analyses of the repaired tissues provided additional insights. Magnified images captured after hematoxylin and eosin (H&E) staining (Fig. 9A) showed that the control group exhibited disorganized tissue rather than normal cartilage within the defect at 6 weeks, while the PPE and PPE μS groups displayed more organized chondrocyte-like cells and cartilage-like tissue ingrowth. By 12 weeks, the PPE and PPE μS groups exhibited near-complete defect repair with smooth surfaces, indicating favorable regeneration. Furthermore, Safranin O/Fast Green and COL2 immunohistochemical staining highlighted stronger positive staining in the PPE μS group, indicating rich GAG and COL2 deposition and newly formed cartilage (Fig. 9A). Notably, COL1 immunohistochemical staining showed a higher content of COL1 in the control group, emphasizing the superior chondrogenic differentiation and COL2 deposition potential of the PPE μS scaffold. In contrast, the control group exhibited disordered fibrocartilage and fibrous tissue growth. Notably, the modified O'Driscoll scores were the highest for the PPE μS group at both 6 weeks (12.67 ± 3.21) and 12 weeks (15.33 ± 1.53) after implantation (Fig. 9B).

For a semiquantitative analysis of cartilage degeneration, we used the OARSI score to observe the effects of treatment with or without scaffolds on the adjacent cartilage. The results showed that the OARSI
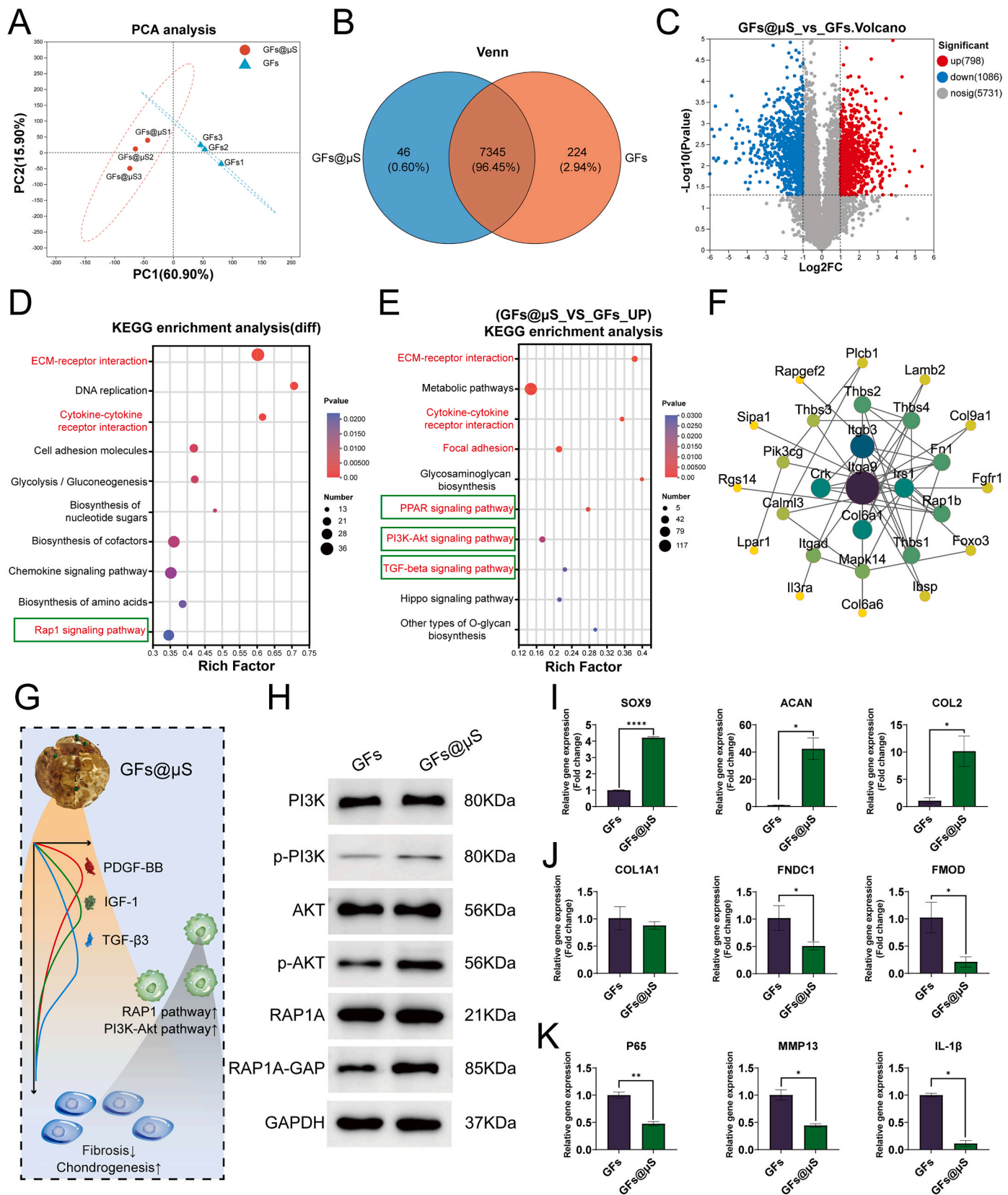
Fig. 7. GFs@μS increase the quality of repaired cartilaginous tissue. A) PCA of DEPs in repaired tissues from the GF group and GFs@μS group. B) Venn diagram of DEPs in the two groups. C) Heatmap of DEPs in the two groups. D) The significantly enriched KEGG terms for the DEPs. E) The significantly downregulated enriched KEGG terms for the DEPs in the two groups. F) PPI network of repaired tissue in the two groups. G) Schematic illustration of GFs@μS-induced cartilage repair. H) Western blot analysis of PI3K-Akt and Rap pathway protein expression. I) Upregulated expression of the chondrogenic genes SOX9, ACAN, and COL2. The expression of (J) fibrous genes COL1, FNDC1, and FMOD and (K) proinflammatory genes, including P65, MMP13, and IL-1β, was downregulated in SMSCs.
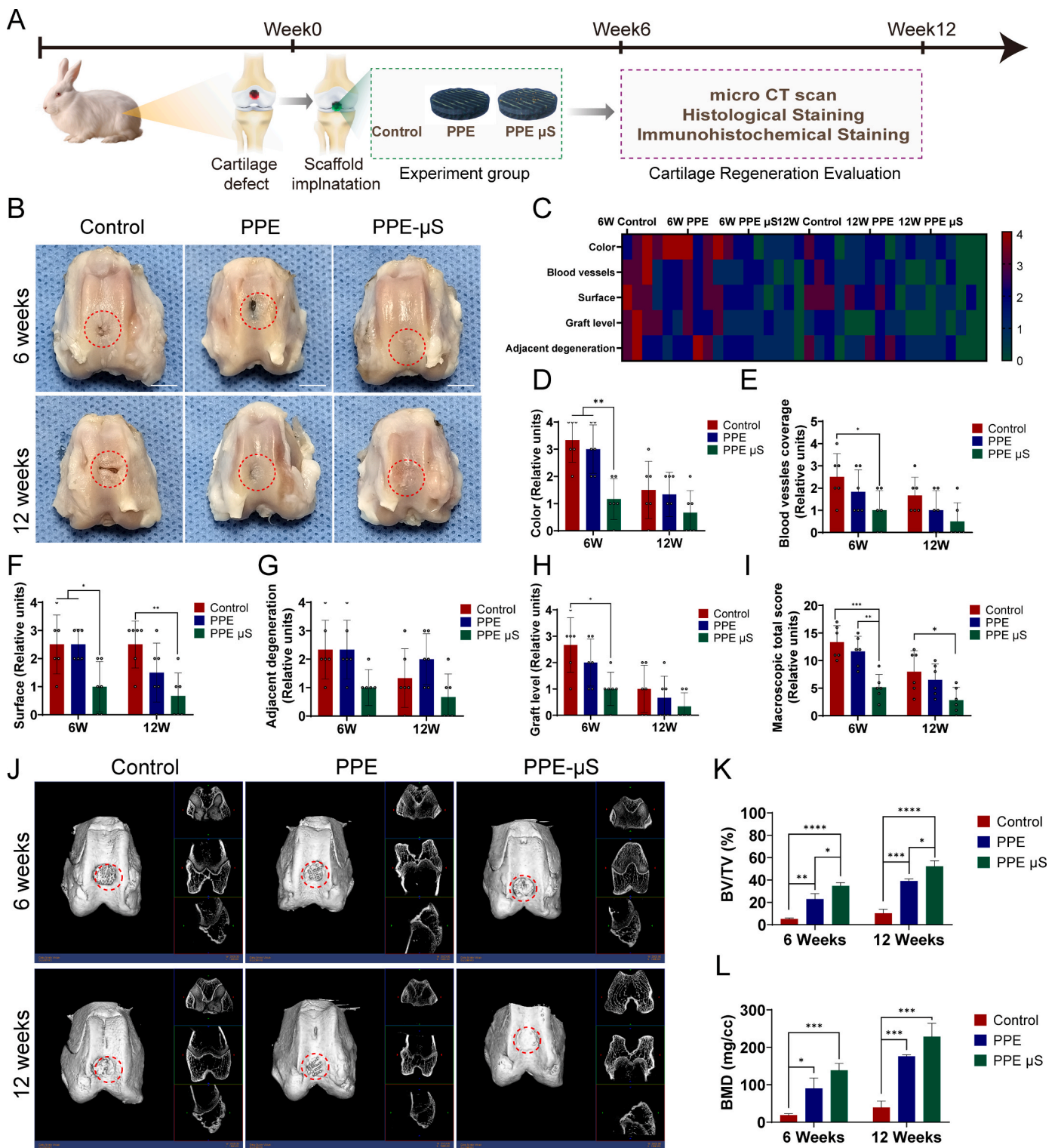
Fig. 8. Macroscopic and micro-CT analyses of cartilage repair after PPE and PPE μS scaffold treatment of cartilage defects at 6 and 12 weeks postoperatively. A) Schematic illustration of the in vivo study design. B) Representative macroscopic images of the repaired tissues at 6 and 12 weeks post-surgery. Red circles indicate the defect areas. C) Heatmap of the macroscopic scoring system. D-I) Comparisons of variables, including color (D), blood vessel coverage (E), surface (F), adjacent cartilage degeneration (G), graft level (H) and the total macroscopic scores (I) among the different groups. J) Micro-CT images showing 2D and 3D reconstructions of the repaired cartilage at 6 and 12 weeks post-surgery. Red circles indicate the defect areas. Quantitative analysis of K) BV/TV and L) BMD in the defect area (n = 3). F) Data are shown as the means ± SDs, n = 6; *p < 0.05, **p < 0.01, ***p < 0.005, and ****p < 0.001.

scores of the periscaffold cartilage in the PPE μS group were better than those in the PPE and control groups at 6 and 12 weeks (P < 0.05) (Fig. 9C). The modified O'Driscoll scores were elevated in the PPE μS group at both 6 weeks (12.67 ± 3.21) and 12 weeks (15.33 ± 1.53) post-implantation (Fig. 9B). Employing the OARSI score to semi-quantitatively analyze cartilage degeneration, the periscaffold cartilage in the PPE μS group showed superior results compared to those in the PPE and control groups at 6 and 12 weeks (P < 0.05) (Fig. 9C).
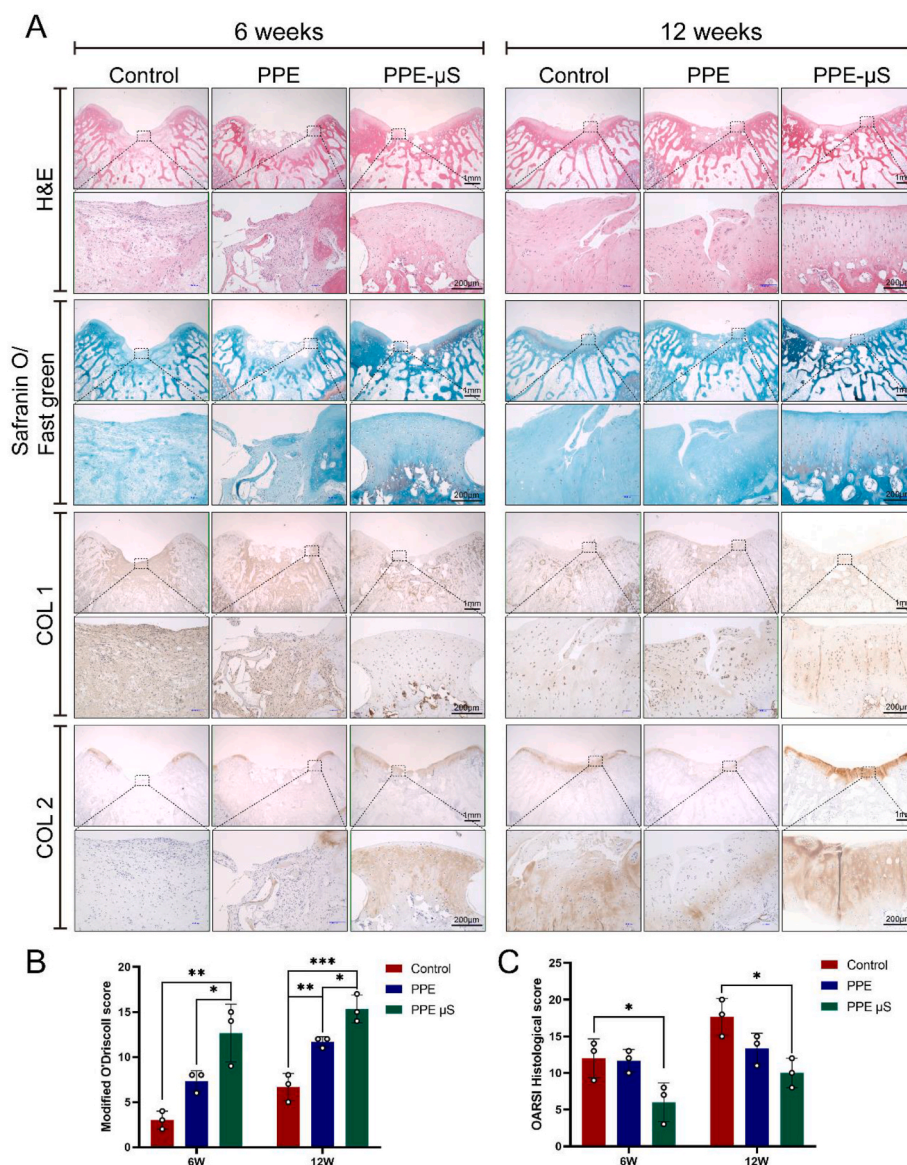
**Fig. 9.** Histological and immunohistochemical assessments of repaired tissues from the control, PPE scaffold and PPE μS scaffold groups in vivo. A) Representative images of H&E (1&2 rows), safranin O/fast green (3&4 rows), and toluidine blue (5&6 rows) staining of repaired cartilage at 6 and 12 weeks and immunohisto-chemical staining for COL1 and COL 2 at 6 and 12 weeks. B) Histomorphology scores of the repaired cartilage tissue at 6 and 12 weeks according to the modified O'Driscoll scoring system. C) OARSI scores of the articular cartilage in each group after 6 weeks and 12 weeks. The data are shown as the means $\pm$ SDs; *$p < 0.05$, **$p < 0.01$, and ***$p < 0.005$.

Furthermore, macroscopic observations and histological analyses of the contralateral patellar cartilage were conducted to assess the protective effects of PPE and PPE μS scaffolds on the rabbit knee joint. Macroscopic observations revealed minimal morphological changes in the PPE μS group, while the PPE and control groups exhibited incomplete and roughened patellar cartilage surfaces (Fig. S9). H&E, SO/FG, and TB staining were used to assess cartilage degeneration in the contralateral patella (Fig. 10A), and the progression of cartilage degeneration was evident across all three groups, with the PPE μS scaffold generating superior chondroprotective effects. The semi-quantitative analysis further confirmed the superiority of the PPE μS scaffold, with significantly better Mankin scores at both 6 and 12 weeks post-implantation (Fig. 10B and C).

3. Discussion

Cartilage regeneration can be categorized into four distinct stages:

the inflammatory and catabolic phase, MSCs recruitment, the anabolic phase, and tissue remodeling [4]. Essentially, emulating these intricate phases is pivotal in formulating advanced tissue engineering strategies. The objective is not only to establish a supportive inflammatory microenvironment surrounding damaged cartilage but also to precisely target multiple stages, mirroring natural biosynthesis processes. This complexity poses a significant challenge in achieving comprehensive cartilage regeneration. In our methodology, we employed microfluidic technology to devise triple GF-loaded composite microspheres complemented with an ACECM-integrated, pDA-modified PCL framework as the foundational scaffold. This procedure resulted in a multifaceted scaffold system tailored as a cell-free solution for chondral defect tissue engineering. The design blueprint of this multifunctional material draws inspiration from the structure of cartilage lacunae and the natural AC repair process. It harnesses the sequential release capabilities of PPE μS to attenuate acute inflammatory reactions while concurrently establishing a chemoattractant gradient to recruit endogenous cells,
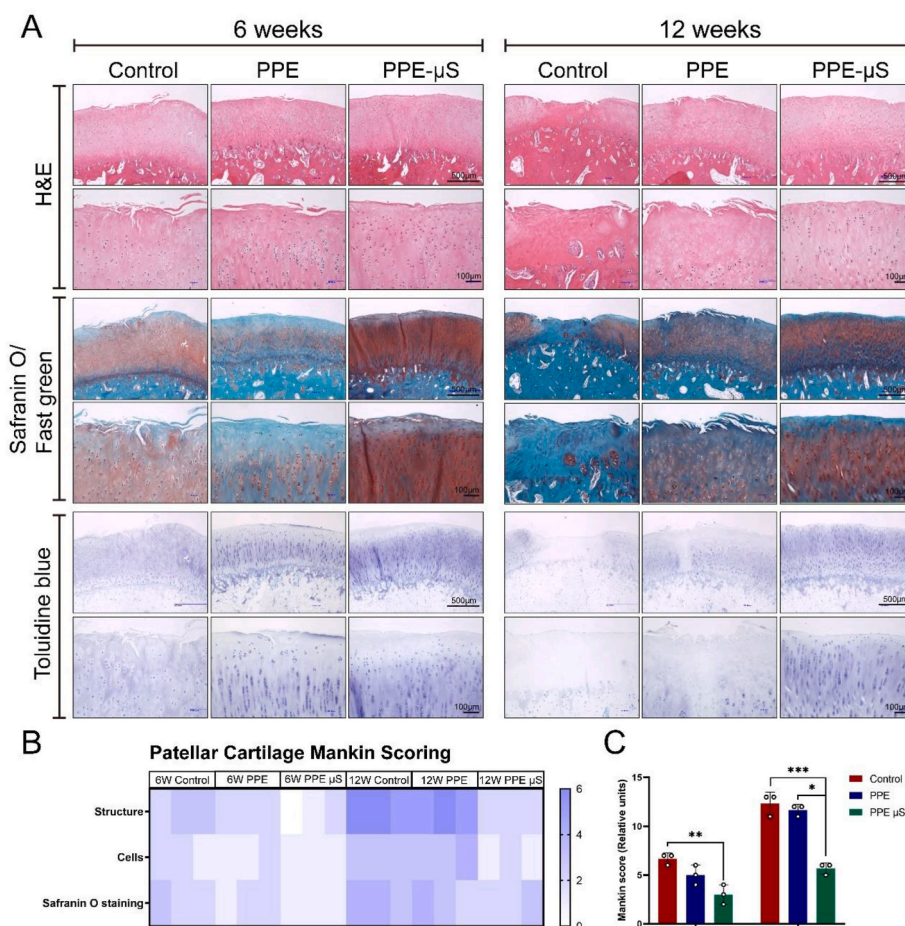
Fig. 10. Analysis of the protective effects of the PPE μS scaffolds on the knees of rabbits with full-thickness chondral defects. A) Histological staining of the patellar cartilage contralateral to the defects. B) Heatmap of the variables used for Mankin histological scoring. C) The total Mankin histological score. The data are shown as the means ± SDs; n = 3; *p < 0.05, **p < 0.01, and ***p < 0.005.

predominantly stem cells, into and toward the GFs@μS to form clusters. Concurrently, the proliferative and chondrogenic factors within the μS establish a conducive microenvironment, favoring stem cell settlement and chondrogenic differentiation.

Following AC injury, inflammatory and subsequent catabolic responses typically occur within the initial days. The intricate nature of the inflammatory process post-cartilage injury, marked by the engagement of multiple inflammatory mediators, complicates therapeutic endeavors aimed at targeting pivotal inflammatory signals that inhibit natural regenerative mechanisms [27]. A protracted inflammatory state induces detrimental pathological processes for cartilage repair, such as M1 macrophage polarization and metalloproteinase secretion. These alterations notably diminish the chondrogenic differentiation capabilities of MSCs and curtail ECM production, resulting in a domino effect culminating in osteoarthritis. Therefore, modulating the AC inflammatory microenvironment has emerged as a crucial therapeutic approach for successful tissue regeneration. Earlier research suggested that fostering appropriate M2 macrophage polarization could be pivotal for enhancing cartilage regeneration and preventing fibrous repair [28,29]. In the quest to mitigate intra-articular inflammation and sustain homeostasis, various nanomaterials and growth factors have been shown to modulate the intra-articular setting toward a conducive environment for chondrogenesis. For instance, Bao et al. reported that polydopamine nanoparticles strongly neutralize reactive oxygen species (ROS) and curtail ROS-induced inflammatory reactions [30]. Hence, in this study, we used IGF-1-embedded pDA nanoparticles to modulate the inflammatory milieu. We employed flow cytometry, RT–qPCR, and

immunofluorescence to detect the surface markers and the genes and proteins expressed by the polarized macrophages to gauge the immunomodulatory capacity of the IGF-1@pDA-laden μS and the amalgamated PPE μS scaffolds. Our initial tests with LPS-stimulated BMDMs and chondrocytes revealed that the IGF-1@pDA-containing μS ameliorated inflammation, inhibited ROS production, and effectively promoted macrophage polarization to the M2 phenotype (Fig. 3A–D). Further assessments revealed a decrease in the number of proinflammatory M1 macrophages and a surge in the number of anti-inflammatory M2 macrophages after the implantation of the PPE μS scaffold into a rat knee AC cartilage defect. In vivo CD86/CD206 immunofluorescence staining further revealed an increase in the number of M2 macrophages during cartilage restoration, underscoring their ability to expedite AC repair within the joint microenvironment (Fig. 3G-L).

Emerging evidence suggests that MSCs mainly exert their therapeutic benefits via paracrine effects. Researchers have posited that proteins and cytokines secreted from MSCs activate surrounding cells to initiate similar biological processes [31]. Although bone marrow stimulation treatments, developed for cartilage repair based on this concept, stimulate stem cells from the bone marrow, their clinical outcomes are unsatisfactory [32]. In the absence of external interventions, such as cell transplantation or scaffold implantation, the body's inherent capacity for endogenous MSCs recruitment and subsequent repair is often inadequate, especially from a long-term perspective [5]. Creating chemoattractant gradients is pivotal for effective stem cell recruitment at injury sites. Hence, we engineered μS with this goal and consistently incorporated PDGF-BB. Our laboratory tests revealed the potential of μS

for sustained release (Fig. 1L) by establishing chemoattractant gradients around the scaffold. This research evaluated MSCs recruitment through engineered μS and PPE μS scaffolds, both in laboratory settings and in live models. Our findings confirmed that the PDGF-BB-loaded μS successfully promoted MSCs migration and recruitment (Fig. 4). However, stem cell migration and recruitment to support cartilage regeneration involve a multifaceted signaling cascade.

Past research has shown that anabolic activities increase over time after AC injury [33]. This result highlights the need for an environment conducive to cartilage regeneration. Notably, during AC healing, cartilage remodeling can deviate due to factors such as angiogenic growth factors (GFs) and osteogenic agents [34,35]. Therefore, guiding tissue remodeling is essential. With their supportive properties, acellular products such as decellularized matrix have become prominent in cartilage regeneration [36]. Our earlier studies emphasized the potential of tissue-derived matrices in guiding cell differentiation and tissue regeneration in vivo [37–39]. Nevertheless, their influence can be limited under extreme post-injury conditions. Recently, multiple drug combinations have been proposed for more effective cartilage regeneration. Fisher et al. illustrated the significance of IGF signaling up to two weeks after chondrogenic induction in MSCs. Here, IGF-1 augments cell growth, inhibiting cell death and potentially aiding in AC repair. Furthermore, the anabolic effects of IGF-1 on cartilage and chondrocytes have been documented [40,41]. Studies have also combined mechano growth factor (MGF) with TGF-β3 to drive the chondrogenic differentiation of MSCs [42]. Consequently, in this study, we introduced TGF-β3 into MSNs to prolong their anabolic activity. Using pellet culture, RT–qPCR, and mRNA sequencing, we assessed the combined effects of these GFs on MSCs.

Our results highlighted the optimal environment for chondrogenic differentiation provided by the PPE μS scaffolds. mRNA sequencing further revealed potential mechanisms by which these scaffolds augment SMSCs chondrogenic differentiation. Multiple signaling pathways orchestrate the chondrogenic differentiation of SMSCs [43,44]. Our mRNA-seq data revealed considerable differences in the DEGs between cells grown on the PPE μS scaffolds and the control scaffolds (Fig. 6). Specifically, pathways related to cell migration, proliferation, and inflammation were notably amplified in the cells grown on PPE μS scaffolds. This finding corroborates previous findings in which the TGFβ-Smad2/3 pathway was identified as crucial for initiating chondrogenesis [45]. Moreover, MAPK family member phosphorylation has been linked to increased Sox9 expression [46]. The PPE μS scaffolds also significantly downregulated inflammation-related pathways, such as the ferroptosis, TNF, NF-κB, IL-17, and NOD-like receptor signaling pathways, suggesting the presence of a more suitable microenvironment for inhibiting inflammation and immune activation [47].

Moreover, in situ cartilage regeneration depends on orchestrated chemical signals to modulate endogenous cells to reconstruct and remodel injured tissue. Previous studies [48,49] have shown that a combination of GFs has long-term positive effects on cartilage regeneration but have not investigated the underlying mechanism in detail. At this time, further investigations of the specific benefits of our specific GF-loaded delivery system for cartilage regeneration should be conducted. Therefore, we incorporated these two types of combinations into ACECM and conducted an in situ cartilage repair assay to examine the different effects of pure GFs with μS and GFs@μS. After 14 days, the repaired tissues were harvested, and a proteomic analysis was conducted. The proteomic results revealed obvious differences in protein levels after the implantation of both hydrogels. The GFs@μS group was supposed to sequentially release GFs, and the repaired tissue exhibited upregulated ECM–receptor, PI3K-Akt, and TGF-beta signaling pathways, which were reported to be positively correlated with cartilage repair [22,50]. Furthermore, the KEGG enrichment analysis suggested that the activation of the Rap1 and PI3K-Akt signaling pathways was potentially correlated with the regeneration of injured cartilage. According to the available evidence, the PI3K/AKT signaling pathway is essential for

normal cartilage development, metabolism, and degradation [22,51]. The Rap1 protein, a member of the Ras superfamily of small GTPases, is regulated by both Rap1 GTPase-activating proteins and Rap1-specific guanine nucleotide exchange factors, which can activate ERK signaling, PI3K/AKT signaling and other downstream pathways [51–53]. Our results showed that RAP1A-GAP may accelerate the transformation of RAP1 from an activated form (combined with GTP) to a deactivated form (combined with GDP) and consequently help activate the PI3K-Akt signaling pathway. Moreover, the in vitro RT–qPCR analysis also showed that the sequential delivery of GFs significantly improved chondrogenesis and reduced fibrosis and matrix degeneration during the SMSCs differentiation process. Based on the above results, GFs@μS treatment effectively activated the expression of RAP1A-GAP, promoted the long-term activation of the Rap1 protein, activated the downstream PI3K/AKT pathway during the induced chondrogenic differentiation of SMSCs, and subsequently improved the quality of the repaired cartilaginous tissue.

Traumatic or chronic damage to the articular cartilage modifies the load-bearing capacity of the joint, leading to abnormal joint loading, fibroblast activation, macrophage activation, and the production of proinflammatory agents, exacerbating cartilage injury [54]. Thus, restoring mechanical equilibrium is critical. In this study, the polymer PCL was 3D printed as a foundation to support ACECM, enhancing the biomechanics of the ECM-based material. Employing a biomimetic extracellular matrix to refine the microenvironment of 3D-printed scaffolds is promising for tissue engineering. Successful integration hinges on creating bonds between the synthetic polymer structure and the surrounding matrix through functional groups or physical interactions [2]. For instance, biocompatible dopamine hydrochloride, inspired by mussels, is increasingly used in synthetic adhesives. These PDA-coated porous scaffolds have shown improved cell adhesion and tissue growth in live models [21,55]. In addition, introducing multiple polyphenol groups may enhance pro-chondrogenic abilities and immunomodulatory effects [56,57]. On the other hand, managing a scaffold's internal pore structure is crucial [58]. Previous studies have shown that the optimal pore size of scaffolds ranges from 100 to 400 μm [59,60]. Bulk hydrogel scaffolds may pose challenges because cell–cell contacts are hindered [61]. Previous research underlines the significance of appropriate pore sizes for chondrogenesis [62]. In this study, we designed scaffolds with specific pore sizes, mirroring collagen scaffolds, which are believed to cater to cell growth, division, and differentiation [63,64]. For practical testing, we assessed the efficacy of the PPE μS scaffold in addressing local chondral defects in rabbits. Macroscopic and microscopic analyses revealed that the PPE μS scaffold was superior to the PPE and control scaffolds in promoting tissue growth, integration, and overall chondral regeneration.

In summary, inspired by the above cartilage repair mechanisms, the multifunctional scaffold developed here is expected to exhibit a desirable ability to regulate macrophages/endogenous MSCs and enhanced mechanical/structural properties. Our findings indicated that the composite scaffold with GFs@μS promoted M2 macrophage polarization and enhanced endogenous stem cell recruitment, proliferation, and chondrogenic differentiation, thereby significantly improving the therapeutic outcome of AC defects. This design emulates the natural repair process of cartilage through the sequential release of PDGF-BB, IGF-1, and TGF-β3. In our strategy, PDGF-BB is initially released to effectively promote the recruitment of SMSCs, followed by the release of IGF-1 to promote protein synthesis and cell proliferation while inhibiting cell death or apoptosis. Finally, TGF-β3 is released to guide the chondrogenic differentiation and maturation of neocartilage cells. Moreover, since early-stage inflammation initiates and activates the repair process, while sustained inflammation can impede subsequent cartilaginous formation, pDA was introduced for surface modification of both the MSNs and the PCL scaffolds due to its moderate ability to modulate the microenvironment. It can indirectly alleviate inflammation by inducing macrophage polarization and serving as an antioxidant to scavenge ROS. This

optimization of the therapeutic process allows a more physiologically congruent approach, thereby enhancing the overall treatment outcome.

However, despite the theoretical advantages of our design, its practical applications may face certain challenges, and the as-prepared scaffold needs further optimization. First, different growth factor types and approaches to precisely control the order and concentration of growth factor release were not compared. PDGF-BB, IGF-1, and TGF-β3 were used in this study since they are the most well-accepted multipotent GFs used in tissue engineering. In addition, our fabricated drug delivery system was not able to temporally release GFs under physiological conditions and was not sufficiently biomimetic compared to the true dynamic dose–time changes in the in vivo cartilage repair process. We need to pay more attention to the evolutionary mechanisms of the key pathophysiological growth factors involved in articular cartilage injury in future studies and design a more bionic multiple slow-release system based on this evolutionary mechanism to improve the efficiency and quality of cartilage repair. Second, as high doses and prolonged delivery of GFs may lead to a loss of effectiveness over time due to the hypertrophy of differentiated chondrocytes [44], other bioactive factors, such as exosomes, small-molecule drugs, or functional peptides, may offer a better solution. Another potential challenge lies in assessing and optimizing the effect of this strategy on the inflammatory and immune microenvironments. Although the designed GFs@μS exhibited enhanced anti-ROS and immunomodulatory effects, their effectiveness could be influenced by numerous factors, including the patient's disease state and overall immune system condition. In view of this situation, Tu et al. developed an anti-inflammatory, antioxidant, and antibacterial conductive hydrogel based on the dynamic crosslinking of a polypeptide, polydopamine and graphene oxide. The combination of these two nanomaterials helped reduce excess ROS levels and activated the polarization of macrophages toward the M2 phenotype, thus significantly promoting diabetic wound repair in vivo [65]. From this point of view, the introduction of new material components is an ideal strategy to enhance the microenvironment-modulating properties of our scaffolds. Last, we also recognize that the scaffold system in this study is too complicated to be applied for clinical translation, as successful clinically translated products usually have simple designs and standardized preparation processes. Thus, while our design strategy appears promising, its practical implementation may require further optimization in terms of fine-tuning the release of growth factors, modulating the microenvironment and rigorous testing to determine whether our scaffold is clinically useful. Overall, more research is needed to evaluate the efficacy and safety of our strategy in real-world clinical settings.

4. Conclusions

This study developed a novel strategy for articular cartilage repair by combining cartilage lacuna-biomimetic hydrogel microspheres with gradual gradient release as a regenerative system and biophysioenhanced PCL/ACECM for a tissue engineering scaffold platform. The engineered GFs@μS and PPE μS scaffolds modulated the cellular inflammatory response and facilitated stem cell recruitment, migration, aggregation, and chondrogenesis. The PPE μS scaffold system presented desirable biocompatibility and physical properties, exploiting the biological functions of ACECM and avoiding its weaknesses via the mechanical properties of the PCL framework. This combination presented superior bioactivities in vitro and in vivo, enabling diverse and balanced therapeutic effects to be achieved during cartilage defect healing in the knee. However, similar to any novel therapy, further research is necessary to optimize the design, assess the long-term effects, and evaluate the performance in larger, more diverse patient populations. Our work provides new directions for further research and a robust platform for the development of advanced therapies for cartilage repair.

5. Materials and methods

5.1. Preparation and characterization of MSNs and MSN@pDA

MSNs were synthesized using a modified Stöber method [66]. Initially, 1.4 g of cetyltrimethyl ammonium bromide (CTAB; Macklin, Shanghai, China) was mixed with 66 mL of deionized water in a beaker and heated to 80 °C in a water bath. After the mixture was clarified, 20 mL of ethyl acetate (Macklin, Shanghai, China) was added, and the solution was magnetically stirred for 30 min. This step was followed by the addition of 14 mL of 1 mol/L NH₄OH, with stirring continuing for an additional 15 min. Then, 7.2 mL of tetraethyl orthosilicate (TEOS; Macklin, Shanghai, China) was added, and the mixture was stirred for 6 h. The resulting porous silica was separated via centrifugation, washed three times with both deionized water and ethanol, dried at 60 °C for 12 h, and calcined at 700 °C for 4 h, yielding MSNs. The morphology and microstructure of the MSNs were analyzed using scanning electron microscopy (SEM; Gemini 300, Zeiss, Germany) and transmission electron microscopy (TEM; Talos F200 X, FEI, Waltham, MA, USA). Particle size was assessed using dynamic light scattering (DLS) on a Zetasizer (Malvern, UK). A protocol reported by Cho et al. [67] was used to load the MSNs with TGF-β3. Briefly, a solution of 860 μL of PBS, 100 μL of TGF-β3 (150 μg/mL), and 40 μL of MSNs (20 mg/mL) was stirred at room temperature for 24 h. The mixture was then centrifuged at 15,000 rpm for 10 min and reconstituted in the exposure medium. For the incorporation of IGF-1 into MSN@pDA, a method adapted from the study by Barati et al. [68] was utilized. In this process, 10 mg of protein-saturated MSNs and 10 μg of IGF-1 were combined in 1 mL of Tris-HCl buffer (pH 8.5) containing 3.0 mg/mL dopamine. This mixture facilitated dopamine polymerization on the MSN surface over a 3-h period. The GF-enriched MSN@pDA was subsequently rinsed with PBS and centrifuged to remove excess protein.

5.2. Microfluidic production of composite microsphere (μS)

Scheme 1 depicts the schematic process for fabricating CS/MSN@pDA μS, which was generated via the method established by Yuan et al. [19]. Briefly, the μS were crafted using a microfluidic approach. First, 200 mg of CS with an average molecular weight of 180 kDa (Shanghai Bio Life Science and Technology Co., Ltd., Shanghai, China) was dissolved in 10 ml of a 0.5 % acetic acid solution to create a 2 % (w/v) CS solution. This solution was then combined with 40 mg of MSN@pDA. After 10 min of ultrasonic agitation, the mixture was passed through a 0.22 μm pore filter to ensure uniformity. This prepared CS/MSN@pDA solution, termed the sample phase, was fed into the microfluidic chip through inlet 2 using pumps. Simultaneously, a 9:1 (v/v) mixture of octane and span 80, acting as the continuous phase, was introduced via inlet 1. This configuration allowed the aqueous CS solution to be segmented into even droplets. These droplets were then immersed in a cross-linking solution (a 2:8 v/v mix of 2.5 % glutaraldehyde and octane) and allowed to set for 30 min to form the μS. After the crosslinking step, the μS were rinsed twice with deionized water and ethanol. A solution containing 200 mg of CS (2 % by weight) and 1 mg of PDGF-BB (100 ng/mL) in 10 mL of water was used to produce CS microspheres containing PDGF-BB. The subsequent fabrication stages mirrored the aforementioned procedure. The loading efficiencies of TGF-β3, IGF-1, and PDGF-BB were measured using the difference method. Briefly, the concentration of the residual GFs retained in the supernatant was quantified using the corresponding ELISA kit (R&D Systems, USA), and the loading efficiency of the GFs was calculated as the differences between the values obtained from the ELISA and the respective initial concentrations of the GFs.

5.3. Physical characterization of the μS

The microstructures and nanostructures of the MSNs, MSN@pDA,

and CS/MSN@pDA were investigated using SEM (S-4800; Hitachi, Tokyo, Japan) and TEM (TALOS F200 X, FEI, Waltham, MA, USA). ImageJ software was used to determine the average diameters of the samples. The chemical groups of MSNs, MSN@pDA, CS/MSNs, and CS/MSN@pDA were characterized using FTIR spectroscopy (Thermo Scientific Nicolet iS5, Waltham, MA, USA). The microspheres were fully submerged in PBS. The plates were then incubated on a shaker at 37 °C. At specific time intervals (spanning 1–8 weeks), the microspheres were dried and weighed. This procedure was conducted in triplicate. The in vitro patterns of PDGF-BB, IGF-1, and TGF-β3 release from the μS were assessed. For the experiment, 5 mg of μS was added to 5 mL of PBS, after which the solution was agitated at 100 rpm and maintained at 37 °C. Over a 29-day period, samples were periodically obtained from the release buffer and preserved at −80 °C for subsequent analysis. The concentrations of PDGF-BB, IGF-1, and TGF-β3 in the supernatant were quantified using the following ELISA kits: PDGF-BB (Neobioscience, Shenzhen, China), IGF-1 (Raybiotech Systems, China), and TGF-β3 (R&D Systems, USA).

5.4. Preparation and characterization of the μS-containing PPE scaffolds

5.4.1. Fabrication of different scaffolds

For μS-containing PPE scaffold (PPE μS) fabrication, we first incorporated μS into ACECM gels at a concentration of 20 mg/mL. Subsequently, the polydopamine-modified PCL scaffolds were immersed in liquid ACECM gel with or without μS, placed in an ultrasonicator for another 2 h and subsequently lyophilized for collection. Finally, the PPE and PPE μS scaffolds were crosslinked using a carbodiimide solution [14 mM 1-ethyl-3-(3-dimethylaminopropyl) carbodiimide hydrochloride (EDAC) and 5.5 mM N-hydroxysuccinimide (NHS); Sigma] for 2 h and sterilized using ethylene oxide. More details on ACECM and PCL scaffold fabrication are provided in the Supporting Information.

5.4.2. Microstructure, pore size and porosity of the scaffold

The macroscopic structures of the scaffolds were visualized using a stereomicroscope (SMZ2; Nikon, Japan). After 24 h of lyophilization, the ultrastructure was examined with a scanning electron microscope (SEM, S-4800; Hitachi, Japan). Before imaging, the samples were sputter-coated with Au for 120 s. The average pore size and porosity were determined using Nano Measure 1.2 (China) and ImageJ (USA) software.

5.4.3. Hydrophilic properties of the scaffolds

The surface hydrophilicity of the scaffolds was assessed using the water contact angle (WCA) method. This assay was conducted with a contact angle goniometer (JY82B; Kruss DSA, Hamburg, Germany) at ambient temperature. A 2 μL droplet of deionized water was placed on the scaffold surface, allowed to settle for 3 s, and visualized using a video contact angle system. Each scaffold was measured five times to obtain an average value.

5.4.4. Mechanical testing of the scaffolds

A compression test was conducted on a microcomputer-controlled electronic universal testing machine to ascertain the biomechanical attributes of the three scaffolds. The scaffolds were $5 \times 5 \times 1.2$ mm long. The precompression specifications were set at 5 %, with a compression rate of 4.5 mm/min and a precompression load of 0.8 N. After 20 initial cycles, the official test was executed with a maximum compression of 10 %. Each scaffold type underwent three tests. The compression moduli were established from the linear fit of the strain–stress curves.

5.4.5. Biocompatibility

The cytocompatibility of the PPE and PPE μS scaffolds was gauged using a live/dead assay kit (Beyotime, Shanghai, China) according to the manufacturer's guidelines. After 3 and 7 days, the cell–scaffold combinations were harvested, rinsed with phosphate-buffered saline (PBS)

twice, and stained with calcein AM and propidium iodide (PI) (Beyotime) for 30 min. After two additional PBS rinses, the samples were viewed under a fluorescence confocal microscope (Leica SP8, Weztlar, Germany). All steps were executed in a light-restricted environment. The morphology of cells cultured on both the PPE and PPE μS scaffolds was inspected through F-actin staining to observe the cytoskeleton. After 3 and 7 days of culture, the cells that adhered to the scaffolds were fixed with 4 % v/v paraformaldehyde for half an hour and then rinsed twice with PBS. Subsequent staining was achieved with FITC-phalloidin (Solarbio, Beijing, China) for 40 min. After another PBS rinse, the cells were exposed to 4′,6-diamidino-2-phenylindole (DAPI; Beyotime, Shanghai, China) for 10 min and visualized with a Leica SP8 fluorescence confocal microscope.

5.5. Evaluation of the anti-inflammatory and immunomodulatory capacities

5.5.1. Anti-inflammatory effects of μS scaffolds on the polarization of macrophages in vitro

The detailed procedures used for the isolation and culture of rat bone marrow-derived macrophages (BMDMs) are available in Supplementary Information Section 1.4. Briefly, rat BMDMs were extracted from 8-week-old male Sprague–Dawley (SD) rats and incubated in DMEM supplemented with macrophage colony-stimulating factor (M-CSF, 40 ng/mL) at a concentration of 5×10^5 cells/well for 6 days. Subsequently, 4×10^5 cells were seeded in a 24-well plate and activated with 10 ng/mL IL-1β and lipopolysaccharide (LPS) for 24 h. Then, four concentrations of CS/MSN@pDA (0, 1, 5, and 10 mg/mL) were added to the medium and cocultured with the activated cells. The resulting conditioned media were labeled as control, CS/MSN@pDA-1, CS/MSN@pDA-2, or CS/MSN@pDA-3. Following a 48-h activation period and washes with PBS, the cells were incubated with fluorophore-conjugated secondary antibodies (goat anti-mouse Alexa Fluor 488, goat anti-rabbit Alexa Fluor 488, goat anti-mouse Alexa Fluor 594 or goat anti-rabbit Alexa Fluor 597, Abcam, UK) at a 1:100 dilution for 1 h at room temperature. After washing the cells again with PBS, the nuclei were counterstained with 4′,6-diamidino-2-phenylindole (DAPI) and examined using a fluorescence microscope (Nikon, Tokyo).

For the RT−qPCR analysis, rat BMDMs were seeded in a 12-well plate (1×10^6 cells/well) with three wells in each group and cultured in DMEM containing 10 ng/mL IL-1β and LPS for 24 h. Then, the experimental groups were cultured in DMEM containing different concentrations of CS/MSN@pDA (0, 1, 5, and 10 mg/mL) (Invitrogen) in accordance with the provided guidelines. The RNA was reverse transcribed to cDNA with a ReverTra Ace qPCR RT Kit (FSQ-201; TOYOBO). The real-time PCR process employed a Step-One Real-Time PCR system and SYBR Green PCR Master Mix (Genestar, USA). The primers used for gene amplification are listed in Table S2 (Supporting Information). GAPDH was used as a reference to normalize target gene expression, and relative expression was determined using the $2^{-\Delta\Delta Ct}$ method. All procedures were performed in triplicate.

For the flow cytometry analysis, the culture conditions were the same as those for the RT−qPCR experiments, and we collected the treated rat BMDMs, digested them with trypsin, and then fixed the cells with 70 % ethanol at 4 °C. Then, the flow cytometry analysis was performed with the help of LIVETRADE (Beijing, China) using the following antibodies: CD45 (E-AB-F1227UJ, Elabscience, China), CD68-PE (130-123-757, Miltenyi, Germany), APC-CD163 (NBP1-43341APC, Novus, USA), and CD86 (200305, BioLegend).

5.5.2. Anti-ROS and chondrocyte-protective effects of CM in vitro

The detailed procedures used for the isolation and culture of rat chondrocytes are available in Supplementary Information Section 1.4. Rat chondrocytes (5×10^5 cells/well) were primed with 10 ng/mL IL-1β and LPS for 24 h. They were subsequently cocultured with various treatments—control, CS/MSN@pDA-1, CS/MSN@pDA-2, and CS/

MSN@pDA-3 in 24-well plates filled with 1 mL of DMEM. After a 12-h coculture, each cell group was rinsed with serum-free culture medium three times. The fluorescent probe 2′,7′-dichlorofluorescein diacetate (DCFH-DA, 10 mM, 1 μL) was then introduced to each set. Following a 20-min incubation, the cells were rinsed three times with PBS. ROS levels were examined using a fluorescence microscope (Nikon, Tokyo). Additionally, rat chondrocytes were seeded in a 12-well plate (5×10^5 cells/well) with three wells in each group and cultured in the above three media for 24 h. The RT−qPCR protocol is described in Section 5.5.1.

5.5.3. Immunomodulatory effects of μS in vivo

All animal trials received approval from the Institutional Animal Care and Use Committee of PLA General Hospital. For the rats, a 2.0-mm-diameter trephine was utilized to create a chondral defect approximately 1 mm deep in the femoral trochlea of the leg, which proceeded until slight bleeding was observed. Immediately, the hydrogels with or without μS were positioned into the defects. The patella was then returned to its place, and the adjacent soft tissue and skin were stitched. Post-surgery, the rats were allowed unrestricted movement and feeding. On the 7th and 14th days post-surgery, the rats from each group were euthanized, and the scaffolds were retrieved. Inflammation levels and in vivo macrophage polarization were gauged through immunofluorescence staining, and images were acquired via CLSM and analyzed quantitatively using ImageJ software.

5.6. In vitro and in vivo cell migration assays

5.6.1. In vitro assays

The wound healing assay serves as a technique to assess cell migration. The detailed procedures used for the isolation and culture of rat SMSCs are available in Supplementary Information Section 1.4. SMSCs were seeded into a 6-well plate at a concentration of 4×10^5 cells per well and cultured at 37 °C in a 5 % CO_2 environment. Once 90 % confluence was achieved, a scratch was made in the cell layer using a 200-μL pipette tip. Afterward, the cells were rinsed three times with sterile PBS to remove cell debris, and the medium was replenished with 0.5 % serum supplemented with PPE and PPE μS scaffolds. Images were recorded at intervals of 0, 12, and 24 h with an inverted microscope. The migration area recovery data were subsequently processed using ImageJ software. The migratory ability of the cells was validated using a Transwell plate (Corning, USA). Briefly, PPE and PPE μS scaffolds were placed in the bottom chamber. Concurrently, 200 μL of an SMSCs suspension (density of 2.5×10^5 cells/mL) was introduced to the top chamber and incubated at 37 °C with 5 % CO_2. Following 16 h of incubation, the chambers were removed, and the cells present on the upper membrane side were meticulously removed with cotton swabs. These cells were then fixed with 4 % PFA for 20 min, followed by staining with a 0.1 % crystal violet solution (Solarbio, Beijing, China). Microscopic observation was subsequently performed, and the results were quantitatively evaluated via ImageJ software.

5.6.2. In vivo assays

Nine six-week-old male SD rats were randomly divided into three distinct groups: the negative control group, the PPE scaffold group, and the PPE μS scaffold group. We generated a rat cartilage defect model, as described in Section 5.5.3, to investigate the potential of the scaffolds for bolstering endogenous MSCs migration in vivo. Seven days after the operation, the rats were euthanized, and the reformed tissue from the defect zone was collected. By identifying CD90 and CD105 as unique MSCs markers, we investigated the effects of the scaffold on SMSCs migration in vivo via immunofluorescence staining. In the procedure, tissue samples were fixed with 4 % paraformaldehyde for 30 min and then permeated with 0.5 % Triton X-100 for an identical duration. After washes with PBS, the samples were treated with an immune blocking solution (Beyotime, Shanghai). Thereafter, the sections were incubated

overnight with primary antibodies against CD90 (1:200, Novus Biologicals) and CD105 (1:100, Novus Biologicals) at 4 °C. This step was succeeded by a 1-h exposure to secondary antibodies conjugated with Alexa Fluor 488 and Fluor 594 (1:100, Abcam, Cambridge, UK) and then a 10-min DAPI (1:200; Beyotime, Shanghai, China) treatment. Cells positive for both CD90 and CD105 were imaged via CLSM, with the quantitative analysis facilitated by ImageJ software.

5.7. Cell proliferation and induced chondrogenic and chondroprotective activities

5.7.1. SMSCs proliferation assay

We used EdU imaging and CCK-8 assays to determine the effects of the scaffolds on SMSCs proliferation. For EdU staining, a Cell-Light EdU in vitro kit (RiboBio, Guangzhou, China) was utilized. SMSCs were cultured on cell slides within a 24-well plate, with an average of 1×10^4 cells per well, for 24 h. Subsequent treatment involved the addition of DMEM/F12 supplemented with 1 % FBS and scaffold extracts for an additional 24 h. The medium was then replaced with a 50 mM EdU solution, and staining for EdU and DNA was conducted using Apollo and Hoechst solutions according to standard protocols. Each staining group comprised three replicates. For the CCK-8 assay, SMSCs were plated in a 96-well plate at 8000 cells per well and cultivated in conventional proliferation medium for 24 h. The original medium was replaced with medium containing scaffold extracts. Following the addition of fresh CCK-8 reagent to each well, a 2-h incubation preceded the measurements. Each concentration was replicated six times.

5.7.2. SMSCs chondrogenesis assay

The chondrogenic differentiation capacity of GFs from the PPE μS scaffold was assessed using a Transwell system (Corning, NY, USA). Initially, 5×10^5 SMSCs were centrifuged at $250 \times g$ for 5 min in a 15 mL tube and then cultured for two days to establish SMSC pellets. The Transwell plates, which were previously used for cell migration experiments, were repurposed for chondrogenic differentiation studies. The pellets were transferred to new medium within the Transwell upper chamber, while the PPE μS scaffold was added to the lower chamber. The chondrogenic culture medium (Cyagen, Santa Clara, CA, USA) was replenished every third day. After 21 days of cultivation, the pellets were documented and analyzed. We conducted an in vitro 3D culture with SMSCs at passage 3 to ascertain the chondrogenic differentiation capabilities of the TCP, PPE scaffold, and PPE μS scaffold. After disinfecting the PPE and PPE μS scaffolds and positioning them in 24-well plates, we seeded SMSCs (5×10^5) at passage 3 onto the scaffolds. The cultivation was performed using chondrogenic induction medium (CIM, Cyagen, Biosciences, China). After 7 and 14 days, the scaffolds were procured and assessed via RT−qPCR. The primers used for the cartilaginous genes are listed in Table S2.

5.7.3. Evaluation of the effect of macrophage-conditioned medium on chondrocyte protection

We evaluated the protective effect of macrophage-conditioned medium after exposure to different scaffolds on chondrocytes using immunofluorescence staining to analyze the expression of IL-1β and MMP-13, which are markers associated with the inflammatory microenvironment. Initially, a 6-well plate was utilized. The different scaffolds (diameter: 5 mm) were placed in the lower chamber, and BMDMs were seeded on the scaffold surface (5×10^5 cells/well). Subsequently, 2 mL of culture medium was added. Chondrocytes were pretreated with 10 ng/mL IL-1β and LPS for 24 h. The upper chamber, with chondrocytes seeded at a density of 5×10^4 cells/well, was then inserted, and an additional 1 mL of culture medium was added. Subsequently, stimuli were applied via fluid exchange, and then, the chondrocytes and BMDMs were cocultured with either PPE or PPE μS scaffolds for 3 days, while the control group did not receive a scaffold. Following the incubation, the chondrocytes were fixed with 4 % paraformaldehyde (PFA),

permeabilized with Triton, and incubated with primary antibodies against IL-1β (1:1000, Abcam, UK) and MMP-13 (1:1000, Abcam, UK) overnight at 4 °C. After washes with PBS, the cells were incubated with secondary antibodies conjugated with Alexa Fluor 488 and 594 (1:1000, Abcam, UK) at room temperature for 1 h. Nuclei were counterstained with DAPI. All experiments were performed in triplicate. Fluorescence images were acquired using a Leica TCS-SP8 confocal microscope (Leica, Germany).

5.8. mRNA-seq analysis

For the mRNA-seq analysis, rat SMSCs at passage 4 were seeded onto PPE μS scaffolds, and chondrogenic induction persisted for 21 days, as described in Section 5.4.1. Simultaneously, the control PPE scaffolds underwent the same chondrogenic induction. After 21 days of induction, the samples were prepared for the mRNA-seq analysis at Shanghai Biotechnology Corporation, Shanghai, China, using next-generation sequencing (NGS) technology on the Illumina NovaSeq 6000 platform. Total RNA was extracted with the RNeasy Micro Kit and purified with the RNA Clean XP Kit and RNase-Free DNase Set. Following library construction, RNA was fragmented and repurposed for cDNA synthesis. A Qubit® 2.0 fluorometer and an Agilent 4200 system were used to measure all the libraries. After determining the fold changes and significance of variances, DEGs with fold changes >1.5 or <0.67 and p values < 0.05 were considered significant. Three independent biological replicates were maintained for each group.

5.9. GFs@μS-induced cartilage regeneration

5.9.1. Proteomic analysis

The animal experimental procedures followed the standards for the care and use of laboratory animals and were approved by the Institutional Animal Care and Use Committee of the Chinese PLA General Hospital. Twelve SD rats were randomly divided into GF (pure GFs mixed with blank μS) and GFs@μS groups. We generated a rat cartilage defect model, as described in Section 5.5.3, to investigate the potential of GFs@μS in bolstering the endogenous regeneration process in vivo. At 14 days post-operation, the rats were euthanized, and the reformed tissue from the defect zone was collected. Then, a label-free proteomic analysis of three regenerated meniscus samples was conducted by the Majorbio Proteomic Service (Shanghai, China) according to the manufacturer's guidelines. Proteins were first extracted and validated using SDS polyacrylamide gel electrophoresis. Subsequently, the digested peptides were analyzed with an EASY-nLC 1200 liquid chromatography–tandem mass spectrometry (LC–MS/MS) system (Thermo Fisher Scientific, USA). The raw data were analyzed with Spectronaut™ software, applying a threshold of a greater than 1.2-fold or less than 0.83-fold change between the PSM-Mg and PSM samples to assess differences in protein expression. For GO and KEGG pathway analyses, the Majorbio Cloud platform (cloud.majorbio.com) [69] was utilized. A comprehensive GO analysis, covering biological processes, cellular components, and molecular functions, was integral to our study.

5.9.2. Western blotting

The cell culture and treatment protocol were the same as those described in Section 5.7.2. After routine protein lysis, denaturation, electrophoresis, and membrane transfer, the membranes were blocked with blocking buffer for 15 min. The membranes were subsequently incubated overnight at 4 °C with the following diluted primary antibodies: anti-β-GAPDH (1:5000, Immunoway, TX, USA), anti-p-PI3K/PI3K (1:2000, Abcam, Cambridge, England), anti-*p*-Akt/Akt (1:1500, Abcam, Cambridge, England), anti-RAP1A (1,500, Abcam), and anti-RAP1A-GAP (1,500, Abcam). The membrane was incubated with the secondary antibody at room temperature, after which the protein bands were visualized.

5.9.3. RT−qPCR

For the evaluation of SMSCs chondrogenic differentiation, SMSCs were cultured with complete chondrogenic differentiation medium (BI, Israel) containing GFs or GFs@μS for 7 days to evaluate the biological effects of these two treatments on the expression of chondrogenic, fibrous, and inflammation-related genes. Total RNA was extracted using a total RNA extraction kit (Vazyme, Nanjing, China). The RNA was then reverse transcribed into cDNA using a reverse transcription kit (Vazyme, Nanjing, China). Real-time quantitative RT−qPCR was performed using SYBR Green I PCR Master Mix. The corresponding primer sequences are listed in Table S2, with the housekeeping gene GAPDH serving as a control.

5.10. In vivo experiment

5.10.1. Surgical procedures

All animal procedures were approved by the Institutional Animal Care and Use Committee of PLA General Hospital. In this study, 24 adult New Zealand white rabbits were categorized into three distinct groups: the PPE scaffold group, PPE μS scaffold group, and an untreated control group. After the animals were anesthetized with pentobarbital sodium, a sterile punch (3.5 mm in diameter and 1.2 mm in depth) was used to produce a chondral defect in the groove of the rabbit knee. Both the PPE scaffold and PPE μS scaffold were then implanted into the defect. The control group was left untreated. Post-surgery, all rabbits received penicillin for three days and were then returned to their respective cages with free movement allowed. Evaluations were conducted at 6 and 12 weeks after the operation.

5.10.2. Gross observation and micro-CT evaluation

The femoral trochlea and patella were visually inspected and photographed. Experienced investigators, working independently and without knowledge of the study groups, assessed the photographs using the macroscopic scoring system from Goebel et al. [70]. The rating parameters are depicted in Table S3. After the macroscopic assessment, the samples were scanned using the GE Explorer Locus SP system. The 3D reconstructions of each femur sample were generated after the scans, and a region of interest (ROI) was delineated in the sample defect regeneration area. Both the bone mineral density (BMD) and the bone volume/tissue volume (BV/TV) of the ROI in each sample were evaluated.

5.10.3. Histological analysis and chondroprotective effect of the scaffolds

After 3 days of fixation in 4 % paraformaldehyde, the samples were decalcified, embedded in paraffin, and sectioned. H&E and Safranin O/Fast Green (SO/FG) staining techniques were used to inspect the repaired cartilage. The histological sections were observed by two independent investigators and semiquantitatively evaluated with the O'Driscoll histological scoring system [24] to evaluate the quality of the repaired tissue and the OARSI scoring system [71] to evaluate cartilage degeneration adjacent to the scaffolds in the chondral defects (Tables S4–5). Immunohistochemical staining procedures for COL2 and COL1 were similarly executed, and the sections were subsequently examined and photographed. The protective efficacy of the scaffolds was gauged through macro-observations and histological analyses of the contralateral patellar cartilage. Following the 6- and 12-week post-operative periods, the patellae were harvested and subjected to H&E, SO/FG, and toluidine blue staining. Histological sections of the contralateral patellar cartilage were semiquantitatively appraised using the Mankin scoring system, as presented in Table S6.

5.11. Statistical analysis

Statistical analyses of parametric data from two groups were performed using Student's *t*-test. Statistical analyses of parametric data from multiple groups were performed using one-way analysis of

variance (ANOVA) followed by Tukey's test. Statistical analyses comparing different groups after different procedures were performed using two-way ANOVA with Tukey's test. The rank-sum test was applied to analyze data with a nonhomogeneous variance. The data were subjected to normality tests, and all analyses were performed using SPSS statistical software (version 25.0, Chicago, IL, USA) or GraphPad Prism 8 software (GraphPad Software Inc., San Diego, CA, USA). All the data are reported as the means ± SDs of the means. Significance was defined as a p value < 0.05.

Data availability statement

The data that support the findings of this study are available from the corresponding author upon reasonable request.

Ethics approval and consent to participate

All animal trials received approval from the Institutional Animal Care and Use Committee of PLA General Hospital.

CRediT authorship contribution statement

Hao Li: Writing – original draft, Conceptualization. **Tianyuan Zhao:** Supervision, Data curation. **Zhiguo Yuan:** Methodology, Investigation. **Tianze Gao:** Visualization, Software. **Yongkang Yang:** Software, Investigation. **Runmeng Li:** Visualization, Software. **Qinyu Tian:** Methodology. **Peifu Tang:** Writing – review & editing. **Quanyi Guo:** Writing – review & editing, Conceptualization. **Licheng Zhang:** Writing – review & editing, Conceptualization.

Declaration of competing interest

All authors involved in this article declare that there are no conflicts of interest regarding the publication of this paper.

Acknowledgments

Appendix A. Supplementary data

Supplementary data to this article can be found online at https://doi.org/10.1016/j.bioactmat.2024.06.037.

List of abbreviations

Abbreviation Definition

TGF-β3   transforming growth factor-β3
MSNs   mesoporous silica nanoparticles
PDGF-BB   platelet-derived growth factor-BB
IGF-1   insulin-like growth factor 1
pDA   polydopamine
CS   chitosan
μS   composite CS/MSN@pDA microspheres
GFs@μS   GFs loaded composite microspheres
ACECM   acellular cartilage extracellular matrix
PCL   polycaprolactone
CS/MSN   chitosan microsphere containing MSNs
MSN@pDA   polydopamine microsphere containing MSNs
CS/MSN@pDA   chitosan microsphere containing MSN@pDA
PPE   polydopamine-modified PCL/ACECM scaffold
PPE μS   polydopamine-modified PCL/ACECM scaffold incorporated

with CMs

References

[1] W. Zhang, C. Ling, A. Zhang, H. Liu, Y. Jiang, X. Li, et al., An all-silk-derived functional nanosphere matrix for sequential biomolecule delivery and in situ osteochondral regeneration, Bioact. Mater. 5 (4) (2020) 832–843.

[2] Y. Li, L. Li, M. Wang, B. Yang, B. Huang, S. Bai, et al., O-alg-THAM/gel hydrogels functionalized with engineered microspheres based on mesenchymal stem cell secretion recruit endogenous stem cells for cartilage repair, Bioact. Mater. 28 (2023) 255–272.

[3] Z. Yang, H. Li, Z. Yuan, L. Fu, S. Jiang, C. Gao, et al., Endogenous cell recruitment strategy for articular cartilage regeneration, Acta Biomater. 114 (2020) 31–52.

[4] T. Zhao, X. Li, H. Li, H. Deng, J. Li, Z. Yang, et al., Advancing drug delivery to articular cartilage: from single to multiple strategies, Acta Pharm. Sin. B. 13 (2022) 4127–4148..

[5] L. Zhou, J. Xu, A. Schwab, W. Tong, J. Xu, L. Zheng, et al., Engineered biochemical cues of regenerative biomaterials to enhance endogenous stem/progenitor cells (ESPCs)-mediated articular cartilage repair, Bioact. Mater. 26 (2023) 490–512.

[6] E.A. Makris, A.H. Gomoll, K.N. Malizos, J.C. Hu, K.A. Athanasiou, Repair and tissue engineering techniques for articular cartilage, Nat. Rev. Rheumatol. 11 (1) (2015) 21–34.

[7] A. Armiento, M. Stoddart, M. Alini, D. Eglin, Biomaterials for articular cartilage tissue engineering: learning from biology, Acta Biomater. 65 (2018) 1–20.

[8] Y.Y. Gong, J.X. Xue, W.J. Zhang, G.D. Zhou, W. Liu, Y. Cao, A sandwich model for engineering cartilage with acellular cartilage sheets and chondrocytes, Biomaterials 32 (9) (2011) 2265–2273.

[9] R.E. Wilusz, J. Sanchez-Adams, F. Guilak, The structure and function of the pericellular matrix of articular cartilage, Matrix Biol. 39 (2014) 25–32.

[10] M. Biondi, F. Ungaro, F. Quaglia, P.A. Netti, Controlled drug delivery in tissue engineering, Adv. Drug Deliv. Rev. 60 (2) (2008) 229–242.

[11] I. Roohani, G.C. Yeo, S.M. Mithieux, A.S. Weiss, Emerging concepts in bone repair and the premise of soft materials, Curr. Opin. Biotechnol. 74 (2022) 220–229.

[12] W. Qiao, H. Xie, J. Fang, J. Shen, W. Li, D. Shen, et al., Sequential activation of heterogeneous macrophage phenotypes is essential for biomaterials-induced bone regeneration, Biomaterials 276 (2021) 121038.

[13] Z. Ma, W. Song, Y. He, H. Li, Multilayer injectable hydrogel system sequentially delivers bioactive substances for each wound healing stage, ACS Appl. Mater. Interfaces 12 (26) (2020) 29787–29806.

[14] F. Wei, S. Liu, M. Chen, G. Tian, K. Zha, Z. Yang, et al., Host response to biomaterials for cartilage tissue engineering: key to remodeling, Front. Bioeng. Biotechnol. 9 (2021) 664592.

[15] S. Muthu, J.V. Korpershoek, E.J. Novais, G.F. Tawy, A.P. Hollander, I. Martin, Failure of cartilage regeneration: emerging hypotheses and related therapeutic strategies, Nat. Rev. Rheumatol. 19 (7) (2023) 403–416.

[16] T. Gonzalez-Fernandez, D.J. Kelly, F.J. O'Brien, Controlled non-viral gene delivery in cartilage and bone repair: current strategies and future directions, Advanced Therapeutics 1 (7) (2018) 1800038.

[17] T. Hodgkinson, D.C. Kelly, C.M. Curtin, F.J. O'Brien, Mechanosignalling in cartilage: an emerging target for the treatment of osteoarthritis, Nat. Rev. Rheumatol. 18 (2) (2022) 67–84.

[18] M.S. Kalairaj, R. Pradhan, W. Saleem, M.M. Smith, A.K. Gaharwar, Intra-articular injectable biomaterials: therapeutic delivery for cartilage repair and regeneration, Adv. Healthcare Mater. (2024) 2303794.

[19] Z. Yuan, Z. Lyu, W. Zhang, J. Zhang, Y. Wang, Porous bioactive prosthesis with chitosan/mesoporous silica nanoparticles microspheres sequentially and sustainedly releasing platelet-derived growth factor-BB and kartogenin: a new treatment strategy for osteoarticular lesions, Front. Bioeng. Biotechnol. 10 (2022) 839120.

[20] A.K. Gaharwar, I. Singh, A. Khademhosseini, Engineered biomaterials for in situ tissue regeneration, Nat. Rev. Mater. 5 (9) (2020) 686–705.

[21] H. Li, T. Zhao, F. Cao, H. Deng, S. He, J. Li, et al., Integrated bioactive scaffold with aptamer-targeted stem cell recruitment and growth factor-induced pro-differentiation effects for anisotropic meniscal regeneration, Bioengineering & Translational Medicine 7 (3) (2022) e10302.

[22] L. Fu, P. Li, J. Zhu, Z. Liao, C. Gao, H. Li, et al., Tetrahedral framework nucleic acids promote the biological functions and related mechanism of synovium-derived mesenchymal stem cells and show improved articular cartilage regeneration activity in situ, Bioact. Mater. 9 (2022) 411–427.

[23] Z. Tianyuan, D. Haoyuan, L. Jianwei, H. Songlin, L. Xu, L. Hao, et al., A smart MMP13-responsive injectable hydrogel with inflammatory diagnostic logic and multiphase therapeutic ability to orchestrate cartilage regeneration, Adv. Funct. Mater. 33 (16) (2023) 2213019.

[24] Z. Yang, T. Zhao, C. Gao, F. Cao, H. Li, Z. Liao, et al., 3D-bioprinted difunctional scaffold for in situ cartilage regeneration based on aptamer-directed cell recruitment and growth factor-enhanced cell chondrogenesis, ACS Appl. Mater. Interfaces 13 (20) (2021) 23369–23383.

[25] Z. Liao, L. Fu, P. Li, J. Wu, X. Yuan, C. Ning, et al., Incorporation of magnesium ions into an aptamer-functionalized ECM bioactive scaffold for articular cartilage regeneration, ACS Appl. Mater. Interfaces 15 (19) (2023) 22944–22958.

[26] G. Tian, S. Jiang, J. Li, F. Wei, X. Li, Y. Ding, et al., Cell-free decellularized cartilage extracellular matrix scaffolds combined with interleukin 4 promote osteochondral repair through immunomodulatory macrophages: in vitro and in vivo preclinical study, Acta Biomater. 127 (2021) 131–145.

[27] R. Liu-Bryan, R. Terkeltaub, Emerging regulators of the inflammatory process in osteoarthritis, Nat. Rev. Rheumatol. 11 (1) (2015) 35–44.

[28] T.A. Wynn, K.M. Vannella, Macrophages in tissue repair, regeneration, and fibrosis, Immunity 44 (3) (2016) 450–462.

[29] Y. Fujihara, T. Abe, K. Hoshi, Controlling the phenotype of macrophages promotes maturation of tissue-engineered cartilage, Tissue Eng. 26 (17–18) (2020) 1005–1013.

[30] X. Bao, J. Zhao, J. Sun, M. Hu, X. Yang, Polydopamine nanoparticles as efficient scavengers for reactive oxygen species in periodontal disease, ACS Nano 12 (9) (2018) 8882–8892.

[31] Y. Han, J. Yang, J. Fang, Y. Zhou, E. Candi, J. Wang, et al., The secretion profile of mesenchymal stem cells and potential applications in treating human diseases, Signal Transduct. Targeted Ther. 7 (1) (2022) 92.

[32] Z. Yang, F. Cao, H. Li, S. He, T. Zhao, H. Deng, et al., Microenvironmentally optimized 3D-printed TGFβ-functionalized scaffolds facilitate endogenous cartilage regeneration in sheep, Acta Biomater. 150 (2022) 181–198.

[33] D.D. Anderson, S. Chubinskaya, F. Guilak, J.A. Martin, T.R. Oegema, S.A. Olson, et al., Post-traumatic osteoarthritis: improved understanding and opportunities for early intervention, J. Orthop. Res. 29 (6) (2011) 802–809.

[34] W. Richter, Mesenchymal stem cells and cartilage in situ regeneration, J. Intern. Med. 266 (4) (2009) 390–405.

[35] W. Zhang, J. Chen, S. Zhang, H.W. Ouyang, Inhibitory function of parathyroid hormone-related protein on chondrocyte hypertrophy: the implication for articular cartilage repair, Arthritis Res. Ther. 14 (4) (2012) 1–10.

[36] Y.S. Kim, M. Majid, A.J. Melchiorri, A.G. Mikos, Applications of decellularized extracellular matrix in bone and cartilage tissue engineering, Bioengineering & translational medicine 4 (1) (2019) 83–95.

[37] L. Hao, Z. Tianyuan, Y. Zhen, C. Fuyang, W. Jiang, Y. Zineng, et al., Biofabrication of cell-free dual drug-releasing biomimetic scaffolds for meniscal regeneration, Biofabrication 14 (1) (2021) 015001.

[38] Z. Yang, H. Li, Y. Tian, L. Fu, C. Gao, T. Zhao, et al., Biofunctionalized structure and ingredient mimicking scaffolds achieving recruitment and chondrogenesis for staged cartilage regeneration, Front. Cell Dev. Biol. 9 (2021) 655440.

[39] C. Ning, C. Gao, P. Li, L. Fu, W. Chen, Z. Liao, et al., Dual-phase aligned composite scaffolds loaded with tendon-derived stem cells for achilles tendon repair, Advanced Therapeutics 5 (9) (2022) 2200081.

[40] W.J. O'Connor, T. Botti, S.N. Khan, J.M. Lane, The use of growth factors in cartilage repair, Orthopedic Clinics 31 (3) (2000) 399–409.

[41] M. Shakibaei, C. Seifarth, T. John, M. Rahmanzadeh, A. Mobasheri, Igf-I extends the chondrogenic potential of human articular chondrocytes in vitro: molecular association between Sox9 and Erk1/2, Biochem. Pharmacol. 72 (11) (2006) 1382–1395.

[42] Z. Luo, L. Jiang, Y. Xu, H. Li, W. Xu, S. Wu, et al., Mechano growth factor (MGF) and transforming growth factor (TGF)-β3 functionalized silk scaffolds enhance articular hyaline cartilage regeneration in rabbit model, Biomaterials 52 (2015) 463–475.

[43] M. Wu, G. Chen, Y.-P. Li, TGF-β and BMP signaling in osteoblast, skeletal development, and bone formation, homeostasis and disease, Bone research 4 (1) (2016) 1–21.

[44] L. Zhong, X. Huang, M. Karperien, J.N. Post, The regulatory role of signaling crosstalk in hypertrophy of MSCs and human articular chondrocytes, Int. J. Mol. Sci. 16 (8) (2015) 19225–19247.

[45] E.H. Budi, D. Duan, R. Derynck, Transforming growth factor-β receptors and Smads: regulatory complexity and functional versatility, Trends Cell Biol. 27 (9) (2017) 658–672.

[46] N. Van Gastel, S. Stegen, G. Eelen, S. Schoors, A. Carlier, V.W. Daniëls, et al., Lipid availability determines fate of skeletal progenitor cells via SOX9, Nature 579 (7797) (2020) 111–117.

[47] Z. Yang, B. Wang, W. Liu, X. Li, K. Liang, Z. Fan, et al., In situ self-assembled organoid for osteochondral tissue regeneration with dual functional units, Bioact. Mater. 27 (2023) 200–215.

[48] Z. Mao, X. Bi, C. Wu, Y. Zheng, X. Shu, S. Wu, et al., A cell-free silk fibroin biomaterial strategy promotes in situ cartilage regeneration via programmed releases of bioactive molecules, Adv. Healthcare Mater. 12 (1) (2023) 2201588.

[49] A.R. Martin, J.M. Patel, R.C. Locke, M.R. Eby, K.S. Saleh, M.D. Davidson, et al., Nanofibrous hyaluronic acid scaffolds delivering TGF-β3 and SDF-1α for articular cartilage repair in a large animal model, Acta Biomater. 126 (2021) 170–182.

[50] C. Ye, J. Chen, Y. Qu, H. Qi, Q. Wang, Z. Yang, et al., Naringin in the repair of knee cartilage injury via the TGF-β/ALK5/Smad2/3 signal transduction pathway combined with an acellular dermal matrix, Journal of Orthopaedic Translation 32 (2022) 1–11.

[51] T. Chen, Y. Peng, W. Hu, H. Shi, P. Li, Y. Que, et al., Irisin enhances chondrogenic differentiation of human mesenchymal stem cells via Rap1/PI3K/AKT axis, Stem Cell Res. Ther. 13 (1) (2022) 392.

[52] B. Boettner, L. Van Aelst, Control of cell adhesion dynamics by Rap1 signaling, Curr. Opin. Cell Biol. 21 (5) (2009) 684–693.

[53] S. Shah, E.J. Brock, K. Ji, R.R. Mattingly, Ras and Rap1: a tale of two GTPases, Semin. Cancer Biol. (2019) 29–39. Elsevier.

[54] M. Kapoor, J. Martel-Pelletier, D. Lajeunesse, J.-P. Pelletier, H. Fahmi, Role of proinflammatory cytokines in the pathophysiology of osteoarthritis, Nat. Rev. Rheumatol. 7 (1) (2011) 33–42.

[55] Q. Liu, M. Chen, P. Gu, L. Tong, P. Wang, J. Zhu, et al., Covalently grafted biomimetic matrix reconstructs the regenerative microenvironment of the porous gradient polycaprolactone scaffold to accelerate bone remodeling, Small (2023) 2206960.

[56] P. Wei, Y. Xu, H. Zhang, L. Wang, Continued sustained insulin-releasing PLGA nanoparticles modified 3D-Printed PCL composite scaffolds for osteochondral repair, Chem. Eng. J. 422 (2021) 130051.

[57] X. Liu, W. Chen, B. Shao, X. Zhang, Y. Wang, S. Zhang, et al., Mussel patterned with 4D biodegrading elastomer durably recruits regenerative macrophages to promote regeneration of craniofacial bone, Biomaterials 276 (2021) 120998.

[58] X. Liang, J. Gao, W. Xu, X. Wang, Y. Shen, J. Tang, et al., Structural mechanics of 3D-printed poly (lactic acid) scaffolds with tetragonal, hexagonal and wheel-like designs, Biofabrication 11 (3) (2019) 035009.

[59] L. Cao, B. Cao, C. Lu, G. Wang, L. Yu, J. Ding, An injectable hydrogel formed by in situ cross-linking of glycol chitosan and multi-benzaldehyde functionalized PEG analogues for cartilage tissue engineering, J. Mater. Chem. B 3 (7) (2015) 1268–1280.

[60] Z. Pan, Z. Duan, X. Liu, H. Wang, L. Cao, Y. He, et al., Effect of porosities of bilayered porous scaffolds on spontaneous osteochondral repair in cartilage tissue engineering, Regenerative biomaterials 2 (1) (2015) 9–19.

[61] B.J. Huang, J.C. Hu, K.A. Athanasiou, Cell-based tissue engineering strategies used in the clinical repair of articular cartilage, Biomaterials 98 (2016) 1–22.

[62] J. Gao, X. Ding, X. Yu, X. Chen, X. Zhang, S. Cui, et al., Cell-free bilayered porous scaffolds for osteochondral regeneration fabricated by continuous 3D-printing using nascent physical hydrogel as ink, Adv. Healthcare Mater. 10 (3) (2021) 2001404.

[63] H. Li, Z. Liao, Z. Yang, C. Gao, L. Fu, P. Li, et al., 3D printed poly (ε-caprolactone)/meniscus extracellular matrix composite scaffold functionalized with kartogenin-releasing PLGA microspheres for meniscus tissue engineering, Front. Bioeng. Biotechnol. 9 (2021) 662381.

[64] M. Varley, S. Neelakantan, T. Clyne, J. Dean, R. Brooks, A. Markaki, Cell structure, stiffness and permeability of freeze-dried collagen scaffolds in dry and hydrated states, Acta Biomater. 33 (2016) 166–175.

[65] Z. Tu, M. Chen, M. Wang, Z. Shao, X. Jiang, K. Wang, et al., Engineering bioactive M2 macrophage-polarized anti-inflammatory, antioxidant, and antibacterial scaffolds for rapid angiogenesis and diabetic wound repair, Adv. Funct. Mater. 31 (30) (2021) 2100924.

[66] X. Zhao, C. Hu, G. Pan, W. Cui, Pomegranate-structured electrosprayed microspheres for long-term controlled drug release, Part. Part. Syst. Char. 32 (5) (2015) 529–535.

[67] Y. Cho, R. Shi, A. Ivanisevic, R.B. Borgens, A mesoporous silica nanosphere-based drug delivery system using an electrically conducting polymer, Nanotechnology 20 (27) (2009) 275102.

[68] D. Barati, C. Gegg, F. Yang, Nanoparticle-mediated TGF-β release from microribbon-based hydrogels accelerates stem cell-based cartilage formation in vivo, Ann. Biomed. Eng. 48 (2020) 1971–1981.

[69] Y. Ren, G. Yu, C. Shi, L. Liu, Q. Guo, C. Han, et al., Majorbio Cloud: a one-stop, comprehensive bioinformatic platform for multiomics analyses, IMeta 1 (2) (2022) e12.

[70] L. Goebel, P. Orth, A. Müller, D. Zurakowski, A. Bücker, M. Cucchiarini, et al., Experimental scoring systems for macroscopic articular cartilage repair correlate with the MOCART score assessed by a high-field MRI at 9.4 T–comparative evaluation of five macroscopic scoring systems in a large animal cartilage defect model, Osteoarthritis Cartilage 20 (9) (2012) 1046–1055.

[71] Z. Yuan, T. Long, J. Zhang, Z. Lyu, W. Zhang, X. Meng, et al., 3D printed porous sulfonated polyetheretherketone scaffold for cartilage repair: potential and limitation, Journal of Orthopaedic Translation 33 (2022) 90–106.